ORIGINAL PAPER

Formation mechanisms of macroscopic globules in andesitic glasses from the Izu–Bonin–Mariana forearc (IODP Expedition 352)

Raúl O. C. Fonseca[1] · Lina T. Michely[2] · Maria Kirchenbaur[3] · Julie Prytulak[4] · Jeffrey Ryan[5] · Kerstin Hauke[6] · Felipe P. Leitzke[7] · Renat R. Almeev[3] · Chris S. Marien[8] · Axel Gerdes[9] · Rico Schellhorn[6]

Abstract

The Izu–Bonin–Mariana volcanic arc is situated at a convergent plate margin where subduction initiation triggered the formation of MORB-like forearc basalts as a result of decompression melting and near-trench spreading. International Ocean Discovery Program (IODP) Expedition 352 recovered samples within the forearc basalt stratigraphy that contained unusual macroscopic globular textures hosted in andesitic glass (Unit 6, Hole 1440B). It is unclear how these andesites, which are unique in a stratigraphic sequence dominated by forearc basalts, and the globular textures therein may have formed. Here, we present detailed textural evidence, major and trace element analysis, as well as B and Sr isotope compositions, to investigate the genesis of these globular andesites. Samples consist of K_2O-rich basaltic globules set in a glassy groundmass of andesitic composition. Between these two textural domains a likely hydrated interface of devitrified glass occurs, which, based on textural evidence, seems to be genetically linked to the formation of the globules. The andesitic groundmass is Cl rich (ca. 3000 $\mu g/g$), whereas globules and the interface are Cl poor (ca. 300 $\mu g/g$). Concentrations of fluid-mobile trace elements also appear to be fractionated in that globules and show enrichments in B, K, Rb, Cs, and Tl, but not in Ba and W relative to the andesitic groundmass, whereas the interface shows depletions in the latter, but is enriched in the former. Interestingly, globules and andesitic groundmass have identical Sr isotopic composition within analytical uncertainty ($^{87}Sr/^{86}Sr$ of 0.70580 ± 10), indicating that they likely formed from the same source. However, globules show high $\delta^{11}B$ (ca. $+ 7‰$), whereas their host andesites are isotopically lighter (ca. $- 1‰$), potentially indicating that whatever process led to their formation either introduced heavier B isotopes to the globules, or induced stable isotope fractionation of B between globules and their groundmass. Based on the bulk of the textural information and geochemical data obtained from these samples, we conclude that these andesites likely formed as a result of the assimilation of shallowly altered oceanic crust (AOC) during forearc basaltic magmatism. Assimilation likely introduced radiogenic Sr, as well as heavier B isotopes to comparatively unradiogenic and low $\delta^{11}B$ forearc basalt parental magmas (average $^{87}Sr/^{86}Sr$ of 0.703284). Moreover, the globular textures are consistent with their formation being the result of fluid-melt immiscibility that was potentially induced by the rapid release of water from assimilated AOC whose escape likely formed the interface. If the globular textures present in these samples are indeed the result of fluid-melt immiscibility, then this process led to significant trace element and stable isotope fractionation. The textures and chemical compositions of the globules highlight the need for future experimental studies aimed at investigating the exsolution process with respect to potential trace element and isotopic fractionation in arc magmas that have perhaps not been previously considered.

Communicated by Hans Keppler.

✉ Raúl O. C. Fonseca
raul.fonseca@rub.de

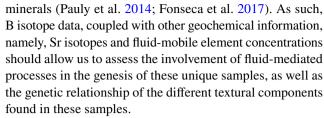Extended author information available on the last page of the article

Introduction

Spheroidal textures, commonly referred to as globules, orbs, orbicules, ocelli, or varioles, are ubiquitous in many magmatic and metamorphic lithologies. However, the exact mechanisms that lead to the formation of spheroidal textures are not well understood and may comprise both primary

and/or secondary processes. Primary magmatic processes invoked to explain spheroidal textures include magma mingling (Polat et al. 2009; Krassivskaya et al. 2009), two-liquid immiscibility (Gélinas et al. 1976; Ferguson and Currie 1972; Philpotts 1982; Asiabanha and Bardintzeff 2013; Ballhaus et al. 2015), and spherulitic crystallization (Philpotts 1977; Sandstå et al. 2011). Non-magmatic processes include devitrification (Lofgren 1971) and alteration of volcanic glasses (Hughes 1977; Hanski 1993), as well as the filling of vesicles that form during degassing by late-stage melts (Smith 1967; Sato 1978; Anderson Jr. et al. 1984). In this framework, unique andesitic samples, recovered during International Ocean Discovery Program (IODP) Expedition 352 to the Izu–Bonin–Mariana forearc, may provide some insights into processes that lead to the formation of spheroidal textures in nature. These samples, which were found in Unit 6 of Hole 1440B during Expedition 352, consist of a complex network of basaltic globules of elipsoidal shape surrounded by a glassy groundmass of andesitic composition. What makes these samples particularly unique is the fact that no other rocks of such evolved andesitic composition were sampled during Expedition 352, where forearc basalts (FAB) and boninites comprise the vast majority of samples recovered (Reagan et al. 2015). These samples are also the only recovered samples that exhibit spheroidal or globular textures, whereas most other samples have been described as being microcrystalline and hyaloclastic in nature (Reagan et al. 2017). Moreover, the FAB sampled during Expedition 352, which surround Unit 6 andesites, are thought to have been produced by decompression melting during subduction initiation without the involvement of recycled subduction components and with little to no fluid flux from the subducted slab (Li et al. 2019; Reagan et al. 2019; Shervais et al. 2019).

Here, we present the results of a detailed petrographic and geochemical study of the globular andesite Unit 6 (Hole 1440B) samples recovered during IODP Expedition 352 to the Izu–Bonin–Mariana forearc to investigate which processes may have led to their formation. What follows is a detailed discussion of how these globular andesites may have formed and the processes, primary or secondary, that can account for the bulk of their textural and geochemical characteristics (and which do not). The toolbox to test these different hypotheses comprises the detailed petrography of the samples, the analyses of their trace element budget, as well as their B and Sr isotope compositions. Boron isotopes, in particular, are well suited to trace processes leading to the formation of these globular samples, as B is soluble in fluids and significant stable isotope fractionation can occur even at magmatic temperatures, especially when compared to the similarly light C or O (Hervig et al. 2002). Boron isotopes are also highly fractionated as a result of low-temperature alteration processes, when adsorbed into secondary clay

minerals (Pauly et al. 2014; Fonseca et al. 2017). As such, B isotope data, coupled with other geochemical information, namely, Sr isotopes and fluid-mobile element concentrations should allow us to assess the involvement of fluid-mediated processes in the genesis of these unique samples, as well as the genetic relationship of the different textural components found in these samples.

Using these data, we have found that the bulk of the textural and geochemical characteristics of the globular andesites from Unit 6 of Hole 1440B IODP Expedition 352 are best explained by fluid-melt immiscibility (also known as degassing) that followed the assimilation of hydrothermally modified forearc basaltic crust that is breaking apart upon subduction initiation. While some other possibilities, like for example, magma mingling and vesicle segregation can explain some of the features of these samples, only fluid-melt immiscibility is consistent with the majority, even if not all of characteristics shown by these unusual globular andesites recovered during IODP Expedition 352.

Geological setting and sampling

The Izu–Bonin–Mariana (IBM) arc system is an active intra-oceanic convergent plate margin trending north-south from Japan to beyond Guam (Fig. 1a; Stern et al. 2003). The arc is around 2800 km long and up to 350 km wide (Stern et al. 2003). The formation of the IBM subduction zone began in the early Eocene and was triggered by a major event of plate reorganization. The very first episode of melting associated with subduction–initiation is generated by adiabatic decompression of mantle upwelling along a foundering Pacific plate resulting from seafloor spreading (Fig. 1b, Reagan et al. 2010; Shervais et al. 2019; Reagan et al. 2019). The firsts melt are MORB-like in composition with a low-to-negligible subduction zone component and have been termed as "forearc basalts" (FAB) (Reagan et al. 2010; Shervais et al. 2018). The FAB and bonitites recovered during Exp. 352 are similar in age and have been dated at 51.34 ±0.78 Ma and 51.27 to 50.33 Ma, respectively (Reagan et al. 2019). Unlike the FAB, boninites show a geochemically significant slab contribution when compared to the FAB (Li et al. 2019). These slab components consists of slab melts, hydrous sediment melts, and fluids from altered oceanic crust (Li et al. 2019).

A primary aim of IODP Expedition 352 was to recover the entire volcanic sequence in the IBM forearc in order to increase our understanding of how subduction zone initiation and the transition towards a mature arc system takes place. Expedition 352 Hole U1440B had a penetration depth of 383.6 metre below the seafloor (mbsf) and recovered exclusively FAB, structurally spanning the range from volcanic extrusives to diabasic dikes. All U1440B units were
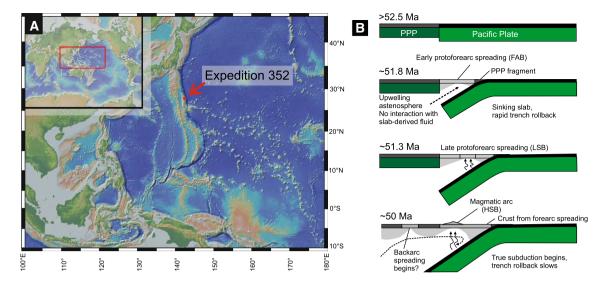
Fig. 1 **a** Topographic map from the Izu–Bonin–Mariana arc. The red arrow shows the approximate location of the drill sites of expedition 352 (Modified from Reagan et al. 2015). **b** Schematic illustration of the Izu–Bonin–Mariana arc formation (after Reagan et al. 2019)

classified as basalts with the exception of Unit 6, which was classified as an andesite, based on both its major element composition and its high-Zr and low-Cr contents. Unit 6 is located within the FAB at around 227 mbsf and has a thickness of approximately 80 cm (Reagan et al. 2015). Unit 6 is exceptional when compared to other units in this Hole, both because of its overall andesitic composition, and because of the presence of complex globular textures, which are the focus of this study. Three glassy andesite samples from Unit 6 were investigated: Samples 352 U1440B 19R 1 W 14/18 cm (short: 19R-1418), 352 U1440B 19R 1 W 27/29 cm (short: 19R-2729), and 352 U1440B 19R 1 W 64/66 cm (short: 19R-6466) (Fig. 2).

Methods

Microscopic petrography and 3D-imaging

Detailed petrography of each sample was carried out using a ZEISS Axio Imager A1m microscope equipped with a Canon PowerShot A640. Samples were imaged under reflected light using both bright-field and dark-field illumination to enhance different textural features of the globules. Specialized software (AutoStich™) was then used to create composite images of each sample, which enabled an overview of the textures of a whole section while retaining microscopic resolution. In order to further characterize the spatial relationship between the textural domains, high-resolution 3D computed X-ray tomography scans were carried out. Samples were scanned using a GE Phoenix|X-ray v|tome|x s equipped with a 240 kV microfocus tube. For a three-dimensional overview of samples 19R-1418 and
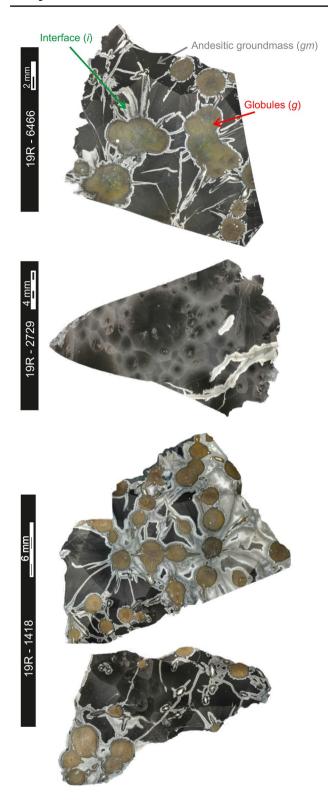
19R-6466, a resolution of 46.999 μm (voxel-size: 0.046999 × 0.046999 × 0.046999 [mm]) ,respectively, and 36.996 μm (voxel-size: 0.036996 × 0.036996 × 0.036996 [mm]) were chosen. Three-dimensional model reconstruction was manually performed using the Avizo Fire 8.1 software package.

Major and trace element analysis

Characterization of the major and minor element contents of each sample was carried out using a JEOL JXA-8200 electron microprobe (University of Bonn) in wavelength dispersive mode (WDS) employing an accelerating voltage of 15 kV and a 15 nA beam current. The electron beam diameter was set between 1 and 25 μm depending on the textural heterogeneity and crystal size. The major and minor element oxides MgO, Na_2O, FeO, K_2O, TiO_2, SiO_2, Al_2O_3, MnO, CaO, P_2O_5, and Cl were quantified. Most of the major element oxides were calibrated on a natural basalt from the Juan de Fuca ridge (VG2 NMNH 111240-52; Jarosewich et al. 1980), while Na_2O was calibrated using a jadeite-diopside eutectic glass, K_2O using sanidine, P_2O_5 apatite, TiO_2 in rutile, and Cl on scapolite (NMNH R6600), employing peak to background calibrations. The ZAF algorithm was used to correct for the different electron absorption properties of the samples, as well as the reference materials used for calibration. Major element concentrations are given as an average of 10–20 representative spots on each measured area. Line scans (quantitative), as well as qualitative X-ray mapping were performed to observe major and minor element variations over the three main textural domains.

Trace element abundances were acquired using a Resonetics Resolution M50-E 193 nm Excimer laser ablation apparatus coupled to a Thermo Scientific X-Series II Q-ICP-MS

Fig. 2 Overview images of samples 19R-1418, 19R-2729 and 19R-7274. Optical microscopy images taken under dark-field illumination were combined to create this overview. All samples exhibit globules surrounded by a andesitic groundmass and a devitrified interface. The exception is sample 19R-2729, which only comprises the andesitic groundmass and minor interfacial material

at the University of Bonn, Germany. On each textural domain, a minimum of 15 spots were carried out using a laser fluence of ~ 6 J/cm^2 and a repetition rate of 15 Hz. The spot size was generally set to 100 μm, with the exception of the interface veins, where the spot size was reduced to 44 μm to avoid contamination from the adjacent andesitic groundmass. For each measured spot, 15 s of background signal were followed by 30 s of ablation signal. Trace element abundances were measured in two separate batches in order to optimize counting statistics and the analytical accuracy and precision of all nuclides measured (cf. method description in Fonseca et al. 2017). This was necessary due to the high number of measured trace elements. The nuclides ^{7}Li, ^{11}B, ^{9}Be, ^{29}Si, ^{31}P, ^{43}Ca, ^{45}Sc, ^{47}Ti, ^{49}Ti, ^{51}V, ^{52}Cr, ^{55}Mn, ^{59}Co, ^{60}Ni, ^{63}Cu, ^{65}Cu, ^{66}Zn, ^{69}Ga, ^{71}Ga, ^{75}As, ^{85}Rb, ^{88}Sr, ^{89}Y, ^{90}Zr, ^{91}Zr, ^{93}Nb, ^{95}Mo, ^{96}Mo, ^{98}Mo, ^{111}Cd, ^{115}In, ^{118}Sn, ^{120}Sn, ^{121}Sb, ^{123}Sb, ^{133}Cs, ^{137}Ba, ^{138}Ba, ^{139}La, ^{140}Ce, ^{141}Pr, ^{146}Nd, ^{147}Sm, ^{151}Eu, ^{153}Eu, ^{157}Gd, ^{159}Tb, ^{163}Dy, ^{165}Ho, ^{166}Er, ^{169}Tm, ^{172}Yb, ^{175}Lu, ^{179}Hf, ^{180}Hf, ^{181}Ta, ^{182}W, ^{184}W, ^{205}Tl, ^{208}Pb, ^{232}Th and ^{238}U were monitored during LA-ICP-MS analysis. NIST-SRM-612 glass (Jochum et al. 2011a) was used as the external standard, with measurements carried out via standard/sample bracketing with no more than 15 spots measured between each standard measurement. Additional spots were carried out in the NIST-SRM-610 glass which was treated as an unknown to check for data accuracy and reproducibility. Concentrations obtained from NIST-SRM-610 were found to be within 5–10% within reported values for that reference material (Jochum et al. 2011a). To correct for differences in ablation efficiency, count rates were normalized to ^{43}Ca as the internal reference standard. Data reduction was carried out employing the methodology described by Longerich et al. (1996).

Boron and Sr isotope analysis

Boron isotope measurements were performed at the Goethe University Frankfurt (GUF) by LA-MC-ICP-MS using USGS GSD-1G glass as the primary reference standard. The MPI DING StHs60/80-G glass and the USGS glass reference materials BHVO and BCR-2G were used as secondary standards for quality control. Representative spot analyses were carried out on all textural domains (globules, andesitic groundmass and interface), as well as on some of the material found filling the vesicles in the samples. A RESOlution (Resonetics) 193nm ArF excimer laser (CompexPro 102, Coherent) equipped with a dual volume S155 laser cell (Laurin Technic, Australia) was used for the ablation of glass samples in a He atmosphere. The sample stream was admixed with Ar and N$_2$ and signals were smoothed using a squid device (Laurin Technic, Australia) prior to introduction into the ICP. The MC-ICP-MS used was a Neptune

(ThermoScientific, Germany) equipped with nine Faraday cups connected to $10^{11}\Omega$ amplifiers. The signal was tuned for maximum ^{11}B sensitivity using standard GUF ICP conditions (e.g. 1280 W RF power, 15.5 L/min cooling gas, 0.8 L/min auxiliary gas) and sample gas flows (0.9 L/min Ar, 0.6 L/min He, and 0.003 L/min N_2). These settings, coupled with a square laser ablation spot size of 200 μm and a depth penetration of 1 μm/s, yielded an ^{11}B signal of ca. 500–800 mV/s on USGS GSD-1G during 26 s of ablation. This value corresponds to an average sensitivity of about 5 V/pg ^{11}B. Instrumental B background was low and uniform during the analytical sessions, with a mean ^{11}B of 0.46 ± 0.08 mV (±1SD) and a mean, mass bias uncorrected $^{11}B/^{10}B$ of 2.9 ± 0.2 (±1SD). The analytical sequence consisted of a series of measurements of the standards (GSD-1G, BHVO, BCR-2G and StHs60/80-G) followed by a block of samples. Every analysis consisted of 28 s of background acquisition, 26 s of sample ablation, and about 20 s between the analysis for signal washout. Spot locations were defined prior to analysis and the laser operated in fully automated mode over the analytical session (50–270 min). Prior to each analysis, the surface was pre-ablated by five laser shots (ca. 0.5 μm of depth) to remove any surface contamination. Laser spots used in each sample analysis typically covered an area of 213 × 213 μm. Laser frequency was set to 10 Hz and the laser energy density to ca. 3 J/cm^2, which resulted in crater depths between 20 and 30 μm during 26 s of ablation. All data treatment was done offline. The average blank level was subtracted from the ^{11}B and ^{10}B intensities and outliers rejected based on the time-resolved $^{11}B/^{10}B$ ratio using a 2σ-test. Correction for mass discrimination (about 11.6%) was accomplished via external calibration using a sample standard bracketing approach (GSD-1G, $\delta^{11}B$ of + 10.1 ‰ ± 0.5, corresponding to $^{11}B/^{10}B$ of 4.0955; Jochum et al. 2011b). GSD-1G was analyzed every 25–30 min and mass discrimination drift (< 1‰ over 60 min) over time was assumed to be linear. The B isotopic composition of the secondary standards was well reproduced for StHs60/80-G ($\delta^{11}B$ of − 4.4 ± 1.0) and BCR2-G ($\delta^{11}B$ of − 5.6 ± 0.7 ‰) when compared to values reported in the literature for the same standards (StHs60/80-G with $\delta^{11}B$ of − 4.5 ± 0.3 ‰, Rosner and Meixner 2004; BCR2-G with a $\delta^{11}B$ of –5.9 ± 0.2 ‰, Gangjian et al. 2013). However, BHVO-2G yielded $\delta^{11}B$ values of − 1.8 ± 1.2 ‰, which are over 1 ‰ lower than the value of − 0.7 ± 0.12 ‰ for BHVO-2 (powder) reported by Gangjian et al. (2013). This offset is likely the result of B isotope heterogeneity of the BHVO-2G glass relative to the powdered sample characterized by Gangjian et al. (2013), as this was the only standard that yielded variable $\delta^{11}B$ over the course of the analytical session, despite having roughly similar B concentrations to BCR2-G (2.5–4.2 μg/g). Boron isotopic compositions are expressed as $\delta^{11}B$ value relative to the boric acid standard SRM 951, using 4.0545 as the reference $^{11}B/^{10}B$ ratio in agreement with Kasemann et al. (2001). Quoted uncertainties are quadratic additions of the within run precision of each analysis and the reproducibility of the GSD-1G glass during the session (SD = 0.2‰, n = 20, Supplementary Table S1).

In addition to the B isotope analysis, the Sr isotopic composition of each textural unit was determined following the procedure described in Marien et al. (2019). Approximately 200 mg aliquots of globule, andesitic groundmass and interface fragmented material were used. Prior to sample digestion, a $^{87}Rb/^{84}Sr$ isotope tracer was added to each aliquot to measure their Sr isotopic composition and Rb and Sr elemental abundances, in order to obtain precise Rb/Sr ratios for later age correction of Sr isotope ratios. Each aliquot was subsequently digested on a hotplate in a 1:1 mixture of conc. HF/conc. HNO_3 for 24–36 h at 120 °C. The solution was subsequently dried down and treated three times with conc. HNO_3 and evaporated to dryness. The dried down sample was taken up in 6 N HCl and equilibrated for 12 h at 120°C. A clear solution was dried down and processed for further ion exchange separation. Strontium separation was carried out using the same aliquot of digested globule, andesitic groundmass and interface aliquots. Strontium was separated from the sample matrix using the method reported by Marien et al. (2019). The Sr isotope composition, and Rb and Sr contents of each aliquot were determined using a Thermo Scientific Neptune MC-ICP-MS located at University of Cologne (Germany). Measured ratios of $^{87}Rb/^{85}Rb$ and $^{87}Sr/^{86}Sr$ were corrected for mass fractionation using the exponential law and normalized to NBS 987 ($^{87}Sr/^{86}Sr$ of 0.710240). Rb-cuts were doped with Zr for mass bias correction and corrected using a $^{91}Zr/^{90}Zr = 0.21795$ (Nebel et al. 2005). Rubidium was measured relative to NBS 984 ($^{87}Rb/^{85}Rb = 0.38554$). Procedural blanks were typically 200 pg for Sr and less than 70 pg for Rb.

Results

Textural relationships

Three textural distinct domains were identified in each sample: an andesitic groundmass (*gm*), that surrounds red brown globules (*g*), and an interface (*i*) surrounding each globule (Fig. 2). The dark grey to black andesitic groundmass is predominantly glassy with small skeletal crystallites at the μm to sub-μm scale (Fig. 3a). Distinct, mostly straight boundaries and triple junctions can be found within the andesitic groundmass where crystallites intersect, forming a "honeycomb" pattern (Fig. 3a). In some areas the crystals seem to have helix-shaped growths (close-up in Fig. 3b). Crystallites

Fig. 3 a Photomicrograph of the andesitic groundmass taken using dark-field illumination, which shows "honeycomb" texture that forms due to the re-orientation of the crystallites. **b** Backscatter electron image (BSE) of skeletal-s to helix–shaped crystallites of clinopyroxene present in the andesitic groundmass. **c** Crystallites often intersect at right angles at the boundaries of "honeycomb" units, forming sharp interfaces

tend to be spherically oriented and converge towards the center of each honeycomb. The boundaries between each honeycomb unit coincide with a sudden change in crystallite orientation, specifically where they intersect at right angles (Fig. 3c).

The red-brownish globules exhibit circular to elliptical cross–sections, vary in size from the sub-mm scale to several mm, and can occur isolated, in clusters, or are aligned like "pearls on a string" (Fig. 2). Globules are texturally heterogeneous and exhibit complex internal micro-fabric, where their outer rim is fine grained, whereas their cores
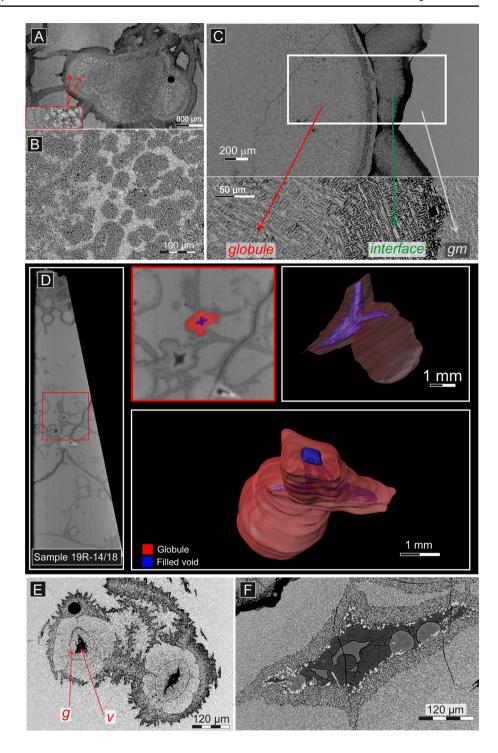
possess an orbicular fabric (Fig. 4a, b). Globules are interconnected to each other via a network of interface veins. In similar fashion to the andesitic groundmass, small skeletal crystallites can be identified within the globules, and radiate towards the globules' surface. The globules are always separated from the andesitic groundmass by a light grey porous interface material (Figs. 2 and 4a). 3D X-ray microtomographic imaging further reveals that globules are almost spherical in shape and appear to have a uniform size distribution, which is not immediately obvious from the 2D sections of the samples (cf. Fig. 4d). Moreover, where they merge (cf. Fig. 2), globules form hollow tubular structures that are filled by similar precipitates as those found in structural voids or vesicles (Fig. 4d). These voids are elongated to spherical in shape, and can occur isolated included in the andesitic groundmass, but more often are found surrounded by a globule with fan-shaped interface areas (Fig. 4e). Voids can vary in size from a few micrometers to several hundreds of micrometers. The mineral precipitates found infilling the voids are very heterogeneous, with spherical-shaped aggregates surrounded by a soft, friable matrix mainly composed of the zeolite phillipsite and clay minerals (Fig. 4f).

The interface (*i*) consists of devitrified andesitic groundmass and is concentrated in areas with high globule density where its spreads radially from the globules (Fig. 2). Globules are, for the most part, entirely surrounded by the interface, with only small slivers of the andesitic groundmass remaining. The contact between the globules and the interface is fan–shaped, and backscatter electron (BSE) images suggest that the interface is compositionally heterogeneous (Fig. 5a). Whereas the boundary between globules and the interface is sharper and plume shaped, the boundary between the interface and the andesitic groundmass tends to be serrated or jagged (Fig. 5b). As in the andesitic groundmass and globules, the interface's groundmass is composed of aligned skeletal crystallites (Fig. 5b). Interestingly, there is no obvious change in the spatial orientation of clinopyroxene crystallites along the transition from the interface to the andesitic groundmass, with only a slight distortion visible between the globules and the other textural domains (Fig. 4c bottom). The interface has lower density than the other textural domains, and because of this it appears darker in the micro-tomographic images (Fig. 5c). Likewise, 3D micro-tomographic imaging reveals that the interface always surrounds and connects globules to form a network of sheet-like veins (Fig. 5c).

Mineral and glass chemistry

The major element composition of all textural domains is given in Table 1. The groundmass is of andesitic composition (60.27 ± 1.16 wt% SiO_2 and 3.19 ± 0.34 wt% MgO) and falls on the arc-tholeiite trend. The near 100% totals

Fig. 4 Backscatter electron (BSE) images of the different textural domains found in the Izu-Bonin samples. **a** isolated globule surrounded by interface material. Red arrows point to the rim of the globule and its inner orbicular texture. Orb formation was very heterogeneous in this globule. Darker roundish orbs are surrounded by a brighter ground mass. **b** Details of the inner orbicular fabric found in the globules. **c** Cross-section of the transition between globule, interface and andesitic groundmass. Crystallite orientation is partially preserved over the three textural domains, albeit with some distortion as they near the globules. **d** 3D micro-tomographic reconstruction of the globules found in sample 19R-14/18, where structural voids (in blue) are always surrounded by semi-spherical globular material (in red). **e** BSE image of a cross-section of structural voids surrounded by globule and interfacial material. **f** BSE image of a structural void that is filled with zeolite and clay material

of the microprobe analysis of the andesitic groundmass, as well as the absence of a clear H_2O band in the Raman spectra obtained from this textural unit (Supplementary Fig. S1) suggest that it contains little to no water (less than 0.1 wt%, which is the detection limit of micro-Raman water analysis—see Fonseca et al. 2017). X-ray diffraction of the andesitic groundmass reveals a degree of crystallinity of around 60 wt% $\pm$ 10. Raman spectroscopy and X-ray

diffraction indicate augite is the only major crystalline phase in the andesitic groundmass (i.e. the crystallites). The Raman spectra obtained from the andesitic groundmass, as well as an augite reference spectrum from the RRuff database (Lafuente et al. 2016) are shown in electronic supplement (Fig. S2A).

The globules are more variable in major element oxide content compared to the andesitic groundmass. This is most

Fig. 5 **a** BSE image of the interface between globules and andesitic groundmass. Often the interface assumes a lobate or fan-like shape expanding outwardly from the globules and into the andesitic groundmass. **b** When interface veins are surrounded by the andesitic ground-mass, the contact between the two textural domains is serrated or jagged. **c** Reconstruction of sample 19R-64/66, where the interface is highlighted (in green), and is known to completely surround the globules (in red)

apparent for SiO_2 ($\pm$ 3.5 wt%), Al_2O_3 ($\pm$ 1.5 wt%), FeO ($\pm$ 4.5 wt%) and K_2O ($\pm$ 1.17 wt%), which is related to their inner orbicular fabric (see Fig. 3a and Table 1), which introduces heterogeneity at the scale of microprobe analysis. Importantly, the globules are enriched in K_2O by a factor of 30 when compared to the andesitic groundmass (0.1 vs. ~ 3 wt%). As with the andesitic groundmass, totals of the microprobe analysis of globules are close to 100 wt% and no water band was visible in the recorded Raman spectra (Supplementary Fig. S1). Moreover, Raman spectroscopy and X-ray diffraction measurements revealed the presence of microcrystalline cpx, as well as alkali feldspar in the globules (see electronic supplement for details). Owing to low totals, and surface charging effects, it was not possible to identify the phases found filling structural voids and vesicles sometimes found included in the globules using the electron microprobe. However, Raman spectroscopic analysis identified the zeolite phillipsite $((Na,K,Ca)_{1-2}(Si,Al)_8O_{16} \cdot 6H_2O)$

and cristobalite as major phases present in these structural voids (See Supplementary Fig. S2). However, identification of the matrix filling these structural voids using Raman spectroscopy was not possible due to pronounced fluorescence. Given the low electron microprobe totals (ca. 80 wt%), and the presence of Mg, Fe and Si, the void-filling matrix likely consists of a mixture of clay minerals.

Electron microprobe measurements of the interface yielded totals of ca. 90 wt% (Table 1). The low electron microprobe totals associated with the interface are consistent with the presence of water or another volatile (e.g. CO_2). However, neither could be confirmed using Raman spectroscopy because background fluorescence was very pronounced, which likely masked the presence of a water or CO_2 band. Notwithstanding the low microprobe totals, the major element composition of the interface is broadly similar to that of the andesitic groundmass. However, it is depleted in Na_2O, as well as Cl by close to a factor of ten

relative to the andesitic groundmass and globules (Table 1 and Fig. 6b). As with the andesitic groundmass and globules, the Raman spectrum of the interface clearly indicates the presence of microcrystalline cpx, but no additional primary or secondary mineral phase was identified.

Trace element data

Nominally fluid-immobile elements like the HREE and the HFSE show little variation between the different textural domains and are similar to the more enriched FAB units recovered in Hole U1440B and Unit 6 andesites from Exp. 352 (Table 2; Fig. 7).

However, globules and andesitic groundmass show distinct negative anomalies in Sr and Ti relative to U1440B FAB and Unit 6 andesites (Li et al. 2019; Shervais et al. 2019, Fig. 7), which is consistent with early fractional crystallization of plagioclase and a Ti-bearing phase (e.g. magnetite). When their trace element contents are normalized relative to the andesitic groundmass, fluid-mobile elements

Fig. 6 Element distribution maps of two chosen areas in the backscattered electron images. Further X-ray maps from additional locations can be found in the supplementary material. **a** X-ray map showing qualitatively the inner globule element variations with the strong differences in the relative element concentration for Si, Al, Fe and K. **b** X-ray map showing qualitatively the concentration differences in the transition area from globule to interface and andesitic groundmass. Interestingly, while potassium has fairly high concentrations within the globules, it is very depleted in the andesitic groundmass. In a similar case, sodium has very low concentrations in the interface when compared to the globules and the andesitic groundmass
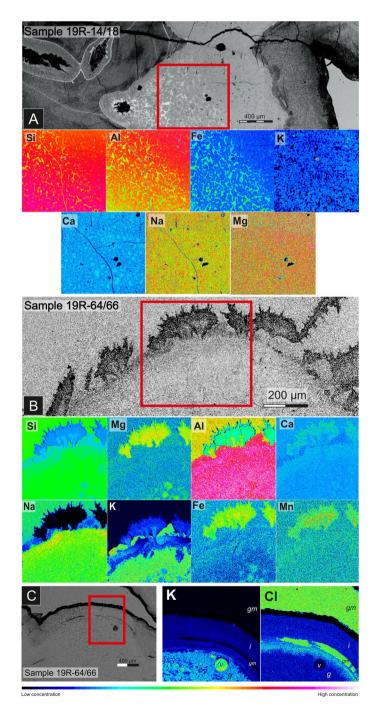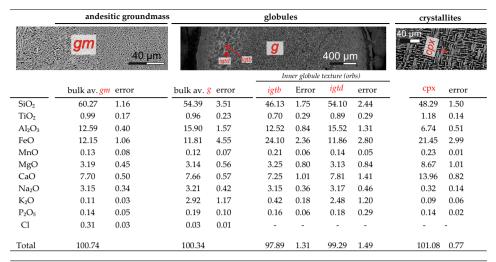
Table 1 Average composition obtained with the EMPA. Major and minor elements were measured as oxides. Abbreviations are listed in the legend of the table. All quoted uncertainties correspond to one standard deviation from the mean value

	andesitic groundmass		globules		Inner globule texture (orbs)				crystallites	
	bulk av. *gm*	error	bulk av. *g*	error	*igtb*	Error	*igtd*	error	*cpx*	error
SiO$_2$	60.27	1.16	54.39	3.51	46.13	1.75	54.10	2.44	48.29	1.50
TiO$_2$	0.99	0.17	0.96	0.23	0.70	0.29	0.89	0.29	1.18	0.14
Al$_2$O$_3$	12.59	0.40	15.90	1.57	12.52	0.84	15.52	1.31	6.74	0.51
FeO	12.15	1.06	11.81	4.55	24.10	2.36	11.86	2.80	21.45	2.99
MnO	0.13	0.08	0.12	0.07	0.21	0.06	0.14	0.05	0.23	0.01
MgO	3.19	0.45	3.14	0.56	3.25	0.80	3.13	0.84	8.67	1.01
CaO	7.70	0.50	7.66	0.57	7.25	1.01	7.81	1.41	13.96	0.82
Na$_2$O	3.15	0.34	3.21	0.42	3.15	0.36	3.17	0.46	0.32	0.14
K$_2$O	0.11	0.03	2.92	1.17	0.42	0.18	2.48	1.20	0.09	0.06
P$_2$O$_5$	0.14	0.05	0.19	0.10	0.16	0.06	0.18	0.29	0.14	0.02
Cl	0.31	0.03	0.03	0.01	-	-	-	-	-	-
Total	100.74		100.34		97.89	1.31	99.29	1.49	101.08	0.77

	interface						voids				
	bulk av. *i*	error	*id*	error	*ib*	error	*vfl*	error	*vfd*	error	*vSiO$_2$*
SiO$_2$	47.29	1.99	44.81	1.18	48.29	0.73	62.09	7.91	54.85	1.34	99.83
TiO$_2$	1.22	0.20	1.41	0.24	1.19	0.10	0.03	0.03	0.10	0.08	0.02
Al$_2$O$_3$	12.57	1.57	11.39	0.72	13.36	0.56	18.86	2.68	21.34	0.55	0.28
FeO	15.03	1.29	16.68	1.02	15.07	0.71	0.11	0.06	0.30	0.08	0.19
MnO	0.19	0.07	0.22	0.05	0.16	0.03	0.02	0.02	0.06	0.03	0.00
MgO	5.72	0.26	5.65	0.40	5.62	0.32	0.04	0.04	4.96	0.30	0.01
CaO	8.07	0.61	8.89	0.95	8.35	0.57	0.55	0.25	1.69	0.10	0.03
Na$_2$O	0.39	0.09	0.45	0.05	0.43	0.07	5.11	1.17	1.01	0.26	0.12
K$_2$O	1.36	0.18	0.98	0.17	1.16	0.12	6.46	1.33	1.77	0.23	0.04
P$_2$O$_5$	0.05	0.02	0.06	0.02	0.05	0.01	0.02	0.01	0.02	0.02	0.00
Cl	0.04	0.02	-	-	-	-	0.02	0.01	0.04	0.02	-
Total	91.92		90.54		93.68		93.32		86.14		100.51

gm andesitic groundmass; *g* globule; *igtb* inner globule texture bright; *ibtd* inner globule texture dark, *cpx* clinopyroxene, *i* interface, *id* interface dark, *ib* interface bright; *vfl* void fill light; *vfd* void fill dark; vSiO$_2$ = void SiO$_2$

show extensive variations in the globules and interface (cf. Fig. 8a). Thallium, B, Rb, and Cs are enriched in the interface and the globules relative to the andesitic groundmass, whereas Ba, P, W, and U are depleted in the interface and are mostly invariant in the globules (Fig. 8a). Lithium is the only element aside from W that displays a slight depletion in the globules but shows a pronounced enrichment in the interface when compared to the andesitic groundmass. The concentration of Sr is relatively constant in all textural domains (Fig. 8a). The light REE are depleted in the interface relative to the andesitic groundmass, but are slightly enriched in the globules (cf. Fig. 8b), whereas the heavy REE show no variation between the different textural domains (Fig. 8b). Fluid-immobile elements like the heavy REE, the HFSE,

Ti and other first row transition elements (V, Cr, Mn and Co—see Fig. 8b, c) show little change between the globules and andesitic groundmass. The interface displays a slight enrichment of all elements after Ti of less than a factor of two (cf. Fig. 8c).

Boron and Sr isotopic composition

The results of the B isotope analysis are shown in Fig. 9 and summarized in Supplementary Table S1. Globules and interface interiors ("bright" in Fig. 9) share the same δ^{11}B, within uncertainty, as well as the most elevated B contents (35 and 97 μg/g B, respectively). The andesitic groundmass is isotopically light, with an average δ^{11}B of

Table 2 Trace element concentrations in μg/g for the different textural domains

Sample	Li	±	B	±	Sc	±	Ti	±	V	±	Cr	±	Mn	±	Ni	±	Co	±	Cu	±	Zn	±	Rb	±	Sr	±	Y	±
19R-6466-gm	13.52	1.07	2.04	0.27	34.68	0.62	5857.24	122	220.61	6.58	52.97	1.63	1721.80	36	41.08	1.96	33.37	1.03	142.33	5.91	166.63	6.21	1.63	0.08	51.47	0.85	65.59	1.56
19R-1418-gm	13.64	0.69	2.19	0.33	34.41	0.54	6511.76	112	199.30	7.11	46.99	1.80	1681.97	47	37.01	2.22	30.53	1.11	20.74	1.01	127.07	9.23	1.75	0.09	53.35	0.67	73.82	1.94
19R-6466-g-1	8.83	0.83	48.27	2.91	34.42	0.37	6303.62	203	217.07	8.47	52.07	1.70	1575.17	84	40.46	2.04	31.77	1.45	50.56	4.26	167.63	6.20	21.07	1.83	59.56	0.92	77.59	3.89
19R-6466-g-2	10.46	1.77	29.53	3.42	33.68	0.72	6478.59	113	215.46	7.97	52.16	2.13	1752.68	54	46.46	2.37	38.15	2.24	56.21	9.98	196.76	12.23	14.37	0.71	57.15	1.03	67.26	1.99
19R-1418-g-1	6.76	1.32	31.56	3.48	32.33	0.88	6061.47	127	183.78	9.03	43.13	2.23	1536.32	41	34.08	1.83	27.67	1.04	22.16	0.99	40.32	7.71	19.40	1.56	56.97	1.28	81.11	5.12
19R-1418-g-2	6.60	0.66	31.68	2.00	32.28	0.88	6217.74	252	198.15	10.24	47.18	2.40	1609.76	53	39.06	2.69	29.21	1.05	24.43	0.78	40.94	6.57	19.79	1.46	55.48	1.31	72.32	2.47
19R-6466-ib	60.01	4.79	96.19	11.19	37.99	1.86	7481.70	612	261.34	14.62	60.62	3.22	2398.63	151	93.94	8.64	0.89	10.41	298.88	70.37	246.56	11.10	22.15	2.42	38.89	2.74	57.99	1.78
19R-1418-ib	60.41	5.67	97.96	14.30	39.14	1.09	8291.81	189	241.01	8.41	57.37	2.17	2291.43	144	75.31	3.64	45.62	5.89	17.71	1.26	263.85	43.57	12.01	1.80	37.60	2.18	64.92	1.90
19R-6466-id	41.01	7.64	63.11	10.69	38.84	0.78	7510.56	315	259.82	10.88	62.75	2.51	2316.17	208	71.94	13.38	84.85	13.86	361.06	162.19	167.55	16.57	11.52	5.13	28.54	5.61	63.70	12.53
19R-1418-id	43.66	6.72	62.61	14.42	38.38	1.64	8245.34	498	250.63	16.77	58.82	4.12	2553.58	232	82.44	11.16	68.21	19.46	16.01	1.91	136.16	60.22	9.99	4.01	30.08	8.91	68.52	2.21

Sample	Zr	±	Nb	±	P	±	Mo	±	In	±	Sn	±	Cs	±	Ba	±	La	±	Ce	±	Pr	±	Nd	±	Sm	±	Eu	±	Gd	±	Tb	±
19R-6466-gm	118.56	3.63	2.96	0.13	1217.73	89	0.157	0.013	0.32	0.005	1.85	0.19	0.22	0.02	14.29	0.03	3.91	0.10	13.62	0.38	2.39	0.06	14.45	0.40	5.53	0.15	1.83	0.05	8.37	0.26	1.52	0.05
19R-1418-gm	135.95	2.57	3.21	0.13	1199.56	64	0.039	0.019	0.28	0.006	1.76	0.18	0.13	0.03	15.59	0.05	4.39	0.10	14.11	0.38	2.56	0.07	15.53	0.51	6.00	0.19	1.96	0.05	9.20	0.30	1.68	0.05
19R-6466-g-1	126.95	6.32	3.40	0.16	1497.51	107	0.079	0.016	0.28	0.008	1.43	0.19	0.23	0.05	10.87	0.06	6.14	0.18	22.76	0.83	3.84	0.41	21.59	2.07	7.82	0.60	2.58	0.19	10.57	0.70	1.87	0.08
19R-6466-g-2	119.18	2.10	3.20	0.11	1226.92	79	0.046	0.012	0.19	0.009	1.36	0.18	0.10	0.04	26.40	0.04	4.66	0.09	18.72	0.76	3.03	0.21	17.36	1.04	6.59	0.34	2.15	0.10	8.87	0.34	1.61	0.06
19R-1418-g-1	125.69	5.19	3.54	0.19	1689.96	220	0.037	0.011	0.23	0.027	1.25	0.17	0.18	0.07	14.72	0.08	6.23	0.19	16.08	0.62	3.49	0.37	20.14	1.77	7.22	0.56	2.34	0.18	10.14	0.77	1.83	0.11
19R-1418-g-2	120.64	3.93	3.58	0.29	1565.00	293	0.040	0.016	0.20	0.029	1.08	0.16	0.23	0.09	14.26	0.04	5.33	0.13	16.31	0.88	3.20	0.25	18.16	0.90	6.67	0.49	2.20	0.16	9.25	0.47	1.66	0.08
19R-6466-ib	160.42	11.18	2.92	0.30	389.95	23	0.095	0.025	0.35	0.070	3.62	0.25	0.44	0.33	3.41	0.06	0.94	0.44	7.11	0.88	1.15	0.16	8.33	0.66	4.20	0.31	1.21	0.11	6.85	0.49	1.34	0.09
19R-1418-ib	177.49	7.08	3.59	0.26	408.74	34	0.067	0.027	0.18	0.047	3.08	0.25	0.46	0.17	2.47	0.04	1.21	0.27	7.57	0.22	1.34	0.09	9.46	0.41	4.82	0.14	1.38	0.09	7.68	0.29	1.47	0.07
19R-6466-id	146.49	17.01	2.90	0.65	443.41	54	0.034	0.017	0.16	0.047	2.19	0.23	0.62	0.17	2.72	0.30	1.05	0.55	5.97	0.71	1.24	0.28	9.01	2.25	4.65	1.03	1.30	0.31	7.64	1.71	1.47	0.36
19R-1418-id	166.00	25.70	3.87	1.57	438.98	59	0.027	0.030	0.18	0.028	2.43	0.25	0.75	0.10	2.48	0.05	1.28	0.70	6.85	0.64	1.39	0.13	9.96	0.76	5.00	0.31	1.42	0.12	8.13	0.42	1.55	0.04

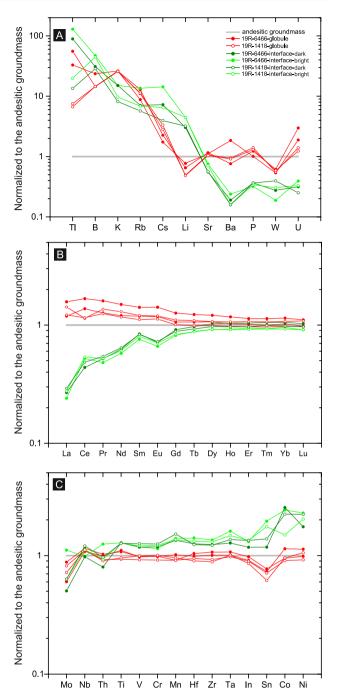| Sample | Dy | ± | Ho | ± | Er | ± | Tm | ± | Yb | ± | Lu | ± | Hf | ± | Ta | ± | W | ± | Tl | ± | Pb | ± | Th | ± | U | ± |
|---|---|---|---|---|---|---|---|---|---|---|---|---|---|---|---|---|---|---|---|---|---|---|---|---|---|---|---|---|
| 19R-6466-gm | 11.19 | 0.27 | 2.46 | 0.05 | 7.48 | 0.18 | 1.14 | 0.04 | 8.13 | 0.17 | 1.21 | 0.04 | 3.73 | 0.10 | 0.18 | 0.01 | 0.04 | 0.010 | 0.01 | 0.008 | 0.67 | 0.127 | 0.23 | 0.0056 | 0.08 | 0.005 |
| 19R-1418-gm | 12.42 | 0.34 | 2.77 | 0.09 | 8.40 | 0.30 | 1.27 | 0.04 | 9.08 | 0.26 | 1.33 | 0.05 | 4.26 | 0.10 | 0.19 | 0.01 | 0.04 | 0.012 | 0.01 | 0.009 | 0.58 | 0.052 | 0.27 | 0.0025 | 0.08 | 0.009 |
| 19R-6466-g-1 | 13.52 | 0.63 | 2.89 | 0.12 | 8.48 | 0.36 | 1.29 | 0.05 | 9.29 | 0.35 | 1.34 | 0.06 | 3.89 | 0.18 | 0.19 | 0.01 | 0.03 | 0.011 | 0.38 | 0.007 | 0.62 | 0.076 | 0.24 | 0.0620 | 0.23 | 0.050 |
| 19R-6466-g-2 | 11.89 | 0.33 | 2.52 | 0.07 | 7.59 | 0.19 | 1.14 | 0.03 | 8.31 | 0.27 | 1.18 | 0.04 | 3.68 | 0.09 | 0.18 | 0.01 | 0.02 | 0.008 | 0.64 | 0.006 | 0.56 | 0.156 | 0.23 | 0.1234 | 0.15 | 0.030 |
| 19R-1418-g-1 | 13.26 | 0.84 | 2.94 | 0.17 | 8.98 | 0.48 | 1.35 | 0.08 | 9.75 | 0.54 | 1.44 | 0.08 | 4.03 | 0.19 | 0.19 | 0.01 | 0.02 | 0.011 | 0.07 | 0.008 | 0.96 | 0.152 | 0.25 | 0.0096 | 0.11 | 0.017 |
| 19R-1418-g-2 | 12.27 | 0.33 | 2.69 | 0.12 | 8.11 | 0.34 | 1.22 | 0.05 | 8.83 | 0.30 | 1.30 | 0.05 | 3.84 | 0.13 | 0.19 | 0.01 | 0.02 | 0.013 | 0.06 | 0.008 | 1.43 | 1.896 | 0.24 | 0.0155 | 0.10 | 0.010 |
| 19R-6466-ib | 10.26 | 0.39 | 2.27 | 0.09 | 7.05 | 0.27 | 1.06 | 0.05 | 7.74 | 0.26 | 1.11 | 0.05 | 5.26 | 0.44 | 0.28 | 0.02 | 0.01 | 0.023 | 1.48 | 0.003 | 0.46 | 0.390 | 0.29 | 0.3206 | 0.03 | 0.015 |
| 19R-1418-ib | 11.43 | 0.34 | 2.52 | 0.08 | 7.72 | 0.24 | 1.18 | 0.05 | 8.39 | 0.24 | 1.22 | 0.05 | 5.60 | 0.27 | 0.28 | 0.02 | 0.01 | 0.024 | 0.19 | 0.009 | 1.60 | 2.208 | 0.25 | 0.0396 | 0.03 | 0.005 |
| 19R-6466-id | 11.49 | 2.57 | 2.56 | 0.60 | 7.74 | 1.88 | 1.20 | 0.30 | 8.55 | 1.79 | 1.24 | 0.30 | 4.70 | 0.55 | 0.22 | 0.03 | 0.01 | 0.049 | 1.02 | 0.009 | 1.59 | 2.143 | 0.19 | 0.3705 | 0.02 | 0.006 |
| 19R-1418-id | 12.05 | 0.27 | 2.68 | 0.08 | 8.10 | 0.22 | 1.26 | 0.05 | 8.90 | 0.30 | 1.29 | 0.05 | 5.27 | 0.70 | 0.26 | 0.02 | 0.02 | 0.057 | 0.13 | 0.010 | 2.13 | 2.462 | 0.26 | 0.0506 | 0.02 | 0.004 |

For abbreviations see legend in the table. All quoted uncertainties correspond to one standard deviation from the mean value. *gm* groundmass; *g* globule; *id* interface dark; *ib* interface bright

Fig. 7 Extended trace element distribution of andesitic groundmass and globules of the Izu-Bonin samples normalized to N-MORB. Values for N-MORB trace element data were taken from Arevalo and McDonough (2010). Trace element data from all Hole U1440B forearc basalt units (FAB), as well as Unit 6 andesite samples are shown for reference (Shervais et al. 2019; Li et al. 2019)

-1‰, albeit with a much larger uncertainty compared to the globules or interface (Fig. 9). The larger variability of andesitic groundmass B isotopic composition compared to the remaining textural domains ($\delta^{11}B = -1 \pm 2.4$ ‰) could be related to its low B abundance (ca. 2 μg/g). However, this possibility is at odds with the excellent reproducibility of the $\delta^{11}B$ of the BCR-2G reference glass material, which has only slightly higher B contents (4.5 μg/g) than the andesitic groundmass. Closer inspection of the individual LA-MC-ICP-MS measurement spots of the andesitic groundmass reveals that it is spatially heterogeneous. Indeed, measurements carried out near the interface display a slight tendency towards more elevated $\delta^{11}B$, which could mean that heavier interfacial material was sampled during the LA-MC-ICP-MS measurements. If these data are excluded, an average $\delta^{11}B$ of -4.9 ± 2.4 ‰ is obtained (Figure 9). However, the variation in $\delta^{11}B$ does not correlate with the B content of the same laser spots in the andesitic groundmass, which is near constant at 2.1 ± 0.3 μg/g. The slightly heavier $\delta^{11}B$ of the andesitic groundmass near the interface relative to the more distal glass domains could be interpreted as the result of diffusive fractionation of B isotopes. However, B diffusion, as measured in haplogranitic melts is very slow and it is thought to result in negligible B isotope fractionation (Chakraborty et al. 1993). It would thus appear that the observed heterogeneity of the B isotopic composition of the andesitic groundmass is unrelated to either contamination by material from the interface or diffusive B isotope fractionation but is rather an intrinsic characteristic of this textural domain.

Fig. 8 Enrichment-depletion diagram: Selected trace elements measured in the globules and the interface normalized to the trace element content of the andesitic groundmass. Trace elements were separated into three groups and are arrange to best display the variations relative to the andesitic groundmass. Closed symbols refer to sample 19R-6466 while open symbols are used for sample 19R-1418

In order to calculate the $^{87}Sr/^{86}Sr_i$ for each textural domain, mass-bias-corrected $^{87}Sr/^{86}Sr$ was corrected assuming an age of 51.34 Ma, which was determined on FAB from Hole 1440B, both above and below Unit 6

Fig. 9 Averages of the B isotope composition ($\delta^{11}B$) obtained for each textural domain in the Unit 6 globular andesite samples versus their measured B concentrations ($\mu g/g$). Average worldwide MORB taken from (Marschall et al. 2017). Quoted uncertainties are given as t-factor 95% confidence level intervals. The B isotope composition of each individual LA-MC-ICP-MS are shown in Supplementary Table S1

(Reagan et al. 2019). Globules and the andesitic groundmass have an almost identical age-corrected $^{87}Sr/^{86}Sr_i$ of 0.705802 (± 9—uncertainty in the last significant digit) and 0.705758 (± 10), respectively, while the interface is clearly more radiogenic than globules and andesitic groundmass with 0.707127 (± 9). Even though care was taken in separating the different textural domains, we cannot exclude the possibility each textural material was contaminated by the others. However, given that the Sr content of all textural domains is broadly similar (41–50 $\mu g/g$), contamination is likely to lead to only relatively small variations in measured $^{87}Sr/^{86}Sr$. All textural domains have Sr isotopic compositions that are significantly more radiogenic than other recovered FAB samples adjacent to Unit 6 (e.g. Unit 3 – 0.703745 $\pm$ 4; Unit 7 – 0.703537 $\pm$ 4; Li et al. 2019).

Discussion

Origin of the Unit 6 andesites

In order to understand how the globular textures found in the Unit 6 andesites have developed, we must first discuss how the andesites themselves have formed. The andesites from Unit 6 are unique in that they are the only occurrence of this lithology in the entire lithostratigraphy recovered during drilling of Hole 1440B and are both preceded and succeeded by FAB (Reagan et al. 2015; Shervais et al. 2019). FAB are assumed to represent the first episode of partial melting after subduction initiation (Reagan et al.

2010; Li et al. 2019; Shervais et al. 2019), and display MORB-like trace element patterns. FAB also show little to no evidence of mass transfer from the slab to the overlying mantle wedge (Reagan et al. 2010), a view supported by recent Hf-Nd-Sr-Pb isotope data (Li et al. 2019). FAB samples from U1440B and Exp. 352 in general show uniformly low fluid—mobile trace element contents (Shervais et al. 2019; Li et al. 2019), which indicates a lack of slab fluid inputs to their mantle sources. The question then arises as to how these unique andesites from Unit 6 formed, and why they have become enriched in fluid-mobile trace elements like Cl, K_2O, and B.

A similar andesitic composition as in the andesitic groundmass can be produced after ca. 75% fractional crystallization from a FAB parental melt has taken place (at 150 MPa—calculated using Rhyolite-MELTS after Gualda et al. 2012; average FAB taken from Shervais et al. 2019). Because presumed FAB water contents average 0.5 wt% (based on LOI data from Shervais et al. 2019), such an andesitic composition would be expected to contain up to 2.4 wt% H_2O after 75% fractional crystallization. LOI values reported for bulk unit 6 andesite samples ranges between 0.35 and 2 wt% (Shervais et al. 2019), values that are consistent with an andesitic melt that resulted from 75% fractional crystallization but that has since degassed and lost some of its water in the process. Even assuming some loss of water due to decompression as the magma ascends to shallower crustal levels (50–100 MPa), an andesitic composition is still expected to have a bit over 1 wt% of water under those conditions (Shishkina et al. 2010), which is at odds with the absence of water from either globules or the andesitic groundmass. Moreover, forearc basalts from U1440B have an average $^{87}Sr/^{86}Sr_i$ of 0.703284 (Li et al. 2019), whereas our Unit 6 globular andesite samples have age-corrected $^{87}Sr/^{86}Sr_i$ of 0.705802 and are, thus, far removed from their presumed parental melts. The formation of Unit 6 globular andesites is therefore unlikely to have resulted from the fractional crystallization of a FAB parental melt alone. The assimilation of altered oceanic crust (AOC) with higher $^{87}Sr/^{86}Sr_i$ may potentially explain the Sr isotopic composition of the andesitic groundmass. Indeed, the elevated Cl/K (>3) of the andesitic groundmass strongly supports the possibility that AOC assimilation has taken place (Bickle and Teagle 1992; Wanless et al. 2010; Harris et al. 2015; Marschall et al. 2017). The range in measured $\delta^{11}B$ across all textural domains (i.e. between -5 and +7) could have been inherited from the assimilation of isotopically heavy AOC (cf. Smith et al. 1995; Brounce et al. 2012; Marschall et al. 2017; Marschall 2018) as it was assimilated by an

isotopically lighter FAB. The globules' elevated K_2O and Tl contents are beyond the level of enrichment expected due to the incompatibility of these elements (Nielsen et al. 2006; Prytulak et al. 2017), while the high $^{87}Sr/^{86}Sr_i$ of 0.705758, and high $\delta^{11}B$ of ca. +7‰ are consistent with the signature of oceanic crust that has been over-printed by hydrothermal activity at shallow crustal levels. An important implication of AOC assimilation is that it would introduce water and other volatile components to an erstwhile volatile-poor forearc magma. A similar process has been invoked by Wanless et al. (2010) to explain the formation of dacites and tholeiitic andesites associated with MORB from the East Pacific Rise, which share many of the characteristics described above (e.g. high K_2O and Cl contents).

Secondary *versus* primary processes

As mentioned previously, globular textures, like the ones exhibited by our samples can be explained by a number of primary (magma mingling, liquid immiscibility), secondary (devitrification, alteration, spherulitic crystallization), and hybrid processes (vesicle segregation). Below, we will discuss the pros and cons of each one of these processes to explain the formation of the Unit 6 Globular andesites, a summary of which can be found in Table 3.

The alteration of volcanic samples can result in spherical structures by taking advantage of pre-existent spherical textures or fabrics, such as large roundish voids, vesicles or spherulites like those depicted in this study. For example, prominent macroscopic varioles found in the flow-banded pillow lava from the Hooggenoeg Complex within the Barberton Greenstone Belt in South Africa are thought to result from the overprint of a pre-existent spherulitic texture during low-grade metamorphism (Sandstå et al. 2011). Spherulitic crystallization is indeed ubiquitous in our samples, yet in this case it did not result in the development of spherical units, but rather in cells with mostly straight to lightly curved contact surfaces redolent of a polygonal or granoblastic texture (see Fig. 3a; for a detailed description of this process refer to the supplementary information). If alteration has been involved in the formation of the globules of this study, it is not associated with spherulitic crystallization. Importantly, the near 100 wt% totals for the electron microprobe analyses of the globules are inconsistent with low-temperature alteration of these samples, which would typically result in the addition of water through de-vitrification and low-temperature alteration of the glass, even if the spherulitic textures were left intact (cf. Lowenstern et al. 2018). Another possibility is that vesicles, which could have originally formed as a result of degassing, were subsequently infilled by an hydrothermal fluid forming the globules. This possibility is highly unlikely, both because it would probably

not result in virtually identical Sr isotopic compositions in both the globules and the andesitic groundmass, and because the likely mode of eruption, in a deep submarine extensional setting associated with the start of subduction (e.g. Shervais et al. 2019), would inhibit vesiculation (cf. Moore 1970; Moore and Schilling 1973; Cichy et al. 2010). There is also no clear evidence that these presumptive vesicles contracted due to degassing, or that resorption of H_2O into melt or globules has taken place (globules and andesitic ground-mass are seemingly anhydrous), which would be expected to result from extensive vesiculation and degassing (McIntosh et al. 2014; Marxer et al. 2015). Low-temperature seafloor alteration of these samples would be expected to introduce elements like Cl and B in addition to water in the form of secondary clays, hydroxy-chlorides and palagonite (Pauly et al. 2014; Seyfried Jr et al. 1986; Gibson et al. 1996). However, Cl is depleted in the globules relative to the andesitic groundmass and, aside from the voids and the interface, and potentially alkali feldspar in the globules, neither textural domain shows evidence of extensive secondary mineralogy. Moreover, although the B concentration of the globules is over a factor of ten higher than in the andesitic groundmass, its isotopic composition is heavier (Fig. 9. The higher $\delta^{11}B$ of the globules compared to the andesitic groundmass is inconsistent with the adsorption of B into secondary clays and palagonite due to low-temperature alteration, which results in an enrichment of lighter ^{10}B (Pauly et al. 2014; Fonseca et al. 2017). It is thus unlikely that the formation of the globules and the andesitic groundmass in the Unit 6 globular andesite can be explained by low-temperature seafloor alteration.

Another possibility that could explain the globular textures found in Unit 6 andesites is that the globules may consist of segregation vesicles (Smith 1967). Segregation vesicles are roundish and elongated structures that are thought to be filled with the residue from the crystallizing magma surrounding them (Smith 1967; Sato 1978). They are thought to result from the migration of that residual liquid through a permeable, already crystalline groundmass, characterized by a rigid network of interlocking crystals (Smith 1967; Anderson Jr et al. 1984). The migration of the residual liquid is driven by the establishment of a pressure gradient due to volatile build-up in a late-stage magma, whereby the liquid is pressed out of the crystalline groundmass into pre-existing vesicles (Anderson Jr. et al. 1984). This process could explain some of the textural characteristics of our samples (e.g. round shape of the globules), and the similarity in the Sr isotope composition of the globules and andesitic groundmass, as they derive from the same parental melt. Moreover, Anderson Jr. et al. (1984) pointed out that material found in these vesicles is often enriched in K_2O relative to the groundmass surround it, which we also see in the relationship between globules and andesitic groundmass. However,

Table 3 List of possible processes that can be used to explain the sum of geochemical and textural characteristics exhibited by the Unit 6 Andesite samples from this study and the pros and cons of each hypothesis

Process	Compositional contrast	Water content	Textural characteristics	Geochemistry
Primary processes				
Magma mingling	Yes. Compositions are similar enough that mingling could occur	Yes. The absence of water is consistent with mingling	No. Mingling does not explain the roundish shape of the globules, nor the presence of a devitrified interface	Inconclusive. Similarity in age corrected Sr isotopes could be explained if both melts are co-genetic. Contrasting B isotope compositions is harder to explain unless one of the melts assimilated AOC
Silicate melt immiscibility	No. SiO_2/FeO ratios are not sufficiently different.	Yes. Given that neither globules or glass matrix have water, this does not invalidate the possibility of silicate melt immiscibility	Inconclusive. This process is consistent with the morphology of the globules, but does not explain the presence of the interface, or the internal orbicular fabric of the globules	No. While consistent with the Sr isotope data, this process is not expected to result in B isotope fractionation, or in the fractionation of fluid-mobile trace elements
Fluid-melt immiscibility (due to degassing)	Inconclusive. Presumed solute composition falls outside of what is expected from experimental studies, where coupled enrichments in Al and Si and depletions in Fe and Mg are expected	Inconclusive. The absence of water from both globules and andesitite groundmass is problematic, as one would not expect degassing to be that efficcient at seafloor pressures (e.g. 50 MPa)	Yes. The globule morphology, its relationship with the andesitic groundmass, and the presence of a devitrified interface are consistent with fluid-melt immiscibility	Yes. Both fluid and conjugate melt are expected to have the same Sr isotope composition once age corrected. Difference in B isotope composition is consistent with fluid-melt equilibria at magmatic temperatures (ca. 800 °C). Fractionation of fluid-mobile elements is also consistent with previous work
Hybrid process				
Segregation vesicles	Yes. The different compositions are entirely consistent with this possibility, albeit one would expect the more evolved composition to segregate into vesicles, not the other way around	Inconclusive. In order for vesiculation to form, some volatile species is required. However, the absence of water from the andesitic groundmass and globules does not rule out the degassing that would be needed for vesiculation to form	No. Typical vesicles are elongated, irregular and submilimetric in size, a far cry from the round-shaped almost cm-sized globules seen in our samples. Also, segregation vesicles are typically restricted to the evolved mesostases of already crystalline rocks	Inconclusive. Similarity in age corrected Sr isotopes could be explained if both melts are co-genetic. Vesicles are often reported to be K_2O-rich. However, contrasting B isotope compositions is harder to explain unless one of the melts assimilated AOC. Why would segregated melts be enriched in some fluid-mobile elements an not others?
Secondary processes				
Spherulitic crystallization	No. Spherulitic crystallization on its own does not result in the establishement of compositional contrasts. These may be established after later alteration	Yes. Loss of water from a melt can result in rapid nucleation and the development of spherulitic crystallization. This process is widespread in the andesitic groundmass, but is not mimicked to the same extent by the globules	Inconclusive. This process is clearly seen in the andesitic groundmass, and it is overprinted by the interface, but it is not observable to the same extent in the globules. Also the globule's internal orbicular fabric is not consistent with the globules resulting from this process	No. Spherulitic crystallization could have made the globules more susceptible to alteration, and thus introduce B and Sr from seawater. However, low-T adsorption of B would introduce light B isotopes, and alteration by seawater does not explain the identical age corrected Sr isotope ratios. Cl- depletion from the globules is also not explainable by spherulitic crystallization

Table 3 (continued)

Process	Compositional contrast	Water content	Textual characteristics	Geochemistry
Devitrification	No. Devitrification on its own does not result in the establishement of compositional contrasts. These may be established after later alteration	No. While devitrification is entirely consistent with the formation of the interface and its presumed higher water contents, it cannot explain the absence of water from the andesitic groundmass of the globules	No. Devitrification is clearly associated with the interface, but not consistent with the textural characteristics of the globules or the andesitic groundmass	No. This process cannot directly account for the geochemical characteristics of the textural domains
Alteration	Inconclusive. While alteration of the andesitic groundmass to form the K_2O-enriched nodules can explain the K_2O-enrichment, it is not consistent with the Cl depletion, nor with the more basaltic character of the globules, and the total absence of H_2O.	No. Aside from the interface, alteration would have been expected to introduce water to at least the globules, coupled to its K_2O-enrichment	Yes. Alteration can result in spherical morphologies, and is consistent with the interface	No. While the heavy B isotope composition of the globules could result from hydrothermal alteration, low-T adsorption of B into secondary clay minerals usually results in lower δ^{11}. Alteration could introduce more radiogenic Sr isotope ratios to the globules, but does not explain why globules and andesitic groundmass have identical age corrected Sr isotope ratios. Low-T alteration is inconsistent Cl loss from the globules and interface

See text for discussion

as stated above, vesiculation is limited at the pressures that prevail on the seafloor (ca. 50 MPa), and any bubbles that form due to degassing at those pressures are sub-millimetre in size and tend to be elongated and irregular in shape (Cichy et al. 2010). However, it should be noted that the small size and irregular shape of such vesicles could also result from shrinkage and deformation during cooling of a fluid-saturated melt (Allabar et al. 2020). Moreover, vesicle shrinkage and their deformation can take place even at fairly rapid cooling rates (e.g. 44 K/s—Marxer et al. 2015; Allabar et al. 2020), so we cannot completely exclude this process from having taken place in our samples. Nevertheless, the relatively large and regular size of the globules in our samples (see Figs. 2, 3) is at odds with this expectation, as well as with depictions of segregation vesicles found in the literature (Anderson Jr. et al. 1984; Sato 1978). In summary, segregation vesicles can only partly explain the formation of the globular andesites from Unit 6.

Two main primary processes might be responsible for the textures found in the globular andesites: magma mingling and silicate melt immiscibility. Structures that result from mingling of two compositionally distinct magmas are generally non-spherical and are best described as streaks or "schlieren" (Snyder et al. 1997). Spherical bodies that result from the mixing of two magma compositions only occur when both liquids have chemical compositions sufficiently disparate to render them immiscible. It is quite clear that the globules found in our samples are close to spherical in shape, suggesting that surface tension between the two compositions was substantially different. Mingling is thus not a viable mechanism. Rather, the globular textures could involve some form of liquid immiscibility (Ballhaus et al. 2015; Drelich et al. 2002; Philpotts 1977).

Silicate melt immiscibility can be invoked to explain the textural characteristics of the globular andesites from Unit 6. The andesitic groundmass and the basaltic globules could represent two immiscible silicate melt compositions, which would be consistent with their similar age corrected Sr isotopic composition. Textures that result from silicate melt immiscibility have been recorded in various rock types, such as tholeiitic basalts, alkaline basalts and occasionally andesites (cf. Sensarma and Palme 2013 and Philpotts 2008). However, these textures are usually restricted to the glassy mesostasis in volcanic rocks, which only form after approximately 75% of fractional crystallization (Philpotts 2008). The andesites found in Unit 6 of Hole U1440B, probably resulted from up to 80% fractional crystallization (Shervais et al. 2019), so a mesostasis could have formed. However, the restricted occurrence of melt immiscibility in association with a mesostasis is hard to reconcile with the globular textures found in our samples for several reasons. Hou and Veksler (2015) have recently reported ferrobasaltic immiscibility products in their experiments at

supraliquidus conditions. However, no natural examples of similar immiscibility products have been reported in either basalts or andesites (Philpotts 2008; Charlier and Grove 2012). Moreover, immiscible melt droplets associated with a mesostasis are exclusively microscopic and rarely exceed 10 µm across (Philpotts 1977, 2008), which is about three orders of magnitude smaller than the globules found in the Unit 6 andesites. The size of the droplets is controlled by the interfacial tension between the immiscible melts (Veksler et al. 2010), which controls the kinetics of phase separation and the textures that form associated with immiscibility (Mungall and Su 2005). The maximum measured interfacial tension between immiscible silicate liquids is low at 16.4 nN/m (Veksler et al. 2010). Low interfacial tension leads to higher nucleation rates of immiscible melt droplets, as well as higher density of these nuclei and a very slow coarsening of the µm to sub-µm droplets (Veksler et al. 2010). Thus, for the millimetre to centimetre-sized globules found in the Unit 6 andesites to form, reduced nucleation and slow cooling rates are required (Philpotts 1977; Veksler et al. 2010), a prerequisite that is at odds with the presence of ubiquitous skeletal-shaped crystals in all textural domains, which generally form as a result of rapid cooling or quenching (cf. Vetere et al. , 2015). Furthermore, major element oxide analyses of immiscible liquid pairs from various volcanic rock samples worldwide, show that the major compositional contrast between the two liquids is their SiO_2/FeO (cf. Philpotts 1982; Veksler et al. 2010; Lester et al. 2013; Sensarma and Palme 2013; Hou and Veksler 2015). For example, in the sample suite studied by Philpotts (1982); Charlier and Grove (2012); Charlier et al. (2013), the immiscible mesostasis and globules found therein have SiO_2/FeO of ca. 20 and ca. 1, respectively. In contrast, the andesitic groundmass and globules found in the Unit 6 andesites are strikingly similar in their SiO_2/FeO, with values of 5 and 4.5, respectively. This clear lack of compositional contrast argues against the possibility that silicate melt immiscibility can explain the formation of the globular andesites. Finally, silicate melt immiscibility would not result in significant B stable isotope fractionation, as B would occur in IV-fold coordination in both melts (Hervig et al. 2002). This expectation is completely at odds with the large difference in the $\delta^{11}B$ exhibited by the andesitic groundmass and globules (-1 and +7‰, respectively). Another process is therefore needed to explain the formation of these globular andesite samples.

Can immiscibility between a hydrous fluid and a fluid-saturated silicate melt explain the globular textures of Unit 6 andesites?

Immiscibility between a hydrous fluid and a fluid-saturated silicate melt has only been recently identified as a potential
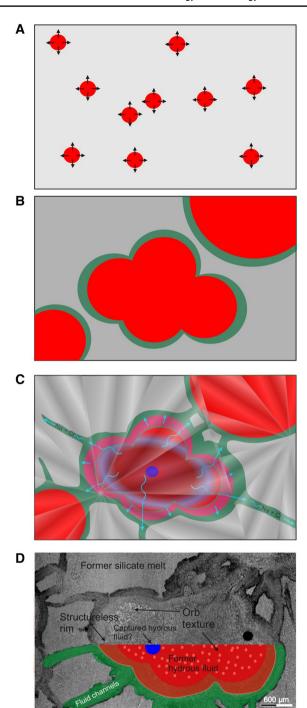
mechanism for the formation of macroscopic globular textures. Known examples include the formation of the globule-rich lavas in the Razjerd district in northern Iran (Asiabanha and Bardintzeff 2013), as well as orbicular textures found in the Troodos ophiolite complex (Ballhaus et al. 2015). Two immiscible liquids are expected to have formed at the onset of fluid saturation, a melt-saturated fluid and a fluid-saturated melt (cf. Ballhaus et al. 2015). Unlike silicate melt immiscibility, the surface tension contrast between a fluid and a silicate melt should be more pronounced (Veksler et al. 2010), which likely promotes an "oil-in-water" type fabric between the two liquids. Within this context, the fluid forms millimetre to centimetre-sized globules surrounded by a silicate melt matrix. Moreover, globules appear to be equidimensional, even when found coalesced together (Fig. 10a), which is a typical feature of immiscible systems (cf. Philpotts , 1977). This expectation is entirely consistent with the morphology of the globules and andesitic groundmass identified via the 3D X-ray micro-tomographic scans shown in Fig. 4. Another strong line of evidence in favour of fluid-melt immiscibility is the observation of crystallites of clinopyroxene across all textural domains. Ballhaus et al. (2015) argued that if at the onset of fluid-melt immiscibility the system is saturated in a given phase (e.g. clinopyroxene) both immiscible fluid and melt should crystallize that phase, which is seen in all textural domains described here in the form of clinopyroxene crystallites. It is also of note that the Sr isotopic composition of the fluid and co-existing melt would, in this scenario, expected to be identical. Moreover, stable B isotope fractionation would be expected to occur as a result of fluid-melt immiscibility. Hervig et al. (2002) argued the equilibrium between a fluid and a basaltic melt could result in fractionation of B isotopes as high as 3‰ at temperatures close to 1100–1200 °C, where the melt would be isotopically lighter than the fluid. Hervig et al. (2002) determined the B isotope fractionation factor between fluid and melt as a function of temperature. If the difference between the $\delta^{11}B$ of globules and andesitic groundmass in our samples of ca. 8‰, is combined with this experimental calibration, it results in a temperature range for fluid-melt immiscibility of around 800–900°C, which would be consistent with a hydrous andesitic melt being completely molten. Moreover, in immiscible silicate melt - fluid systems, fluid-mobile elements like K, Na, Rb, Cs and Li can fractionate from each other (Veksler 2004). Taken at face value, this seems to be reflected by the distribution of fluid-mobile elements in our globular andesite samples, where K, Tl, B, Rb and Cs show distinct enrichments in the globules relative to the andesitic groundmass, while Na, Ba and Sr are similar in both textural domains (cf. Fig. 8a).

Assuming the globular andesites formed due to fluid exsolution, we can recreate the sequence of events that may have led to their formation. Given that there is little evidence

Fig. 10 a Exsolution of a hydrous solute-bearing fluid from a silicate melt. Exsolution of equidimensional fluid droplets is triggered by decompression of an erstwhile water–saturated magma. **b** With increasing decompression, the immiscible fluid droplets grow and begin to coalesce. However, the immiscible fluid globules likely sustain water loss, to the extent that a water-rich phase will separate from the "solute" and potentially starts to escape. **c** The separation and extraction of the water-rich fluid from the system leads to a rapid undercooling of the systems which in turn triggers spherulitic crystallization. The interface likely formed at the same time as a result of fluid escape, and results from the interaction between the escaping fluid and the "silicate melt" or quenched glass. The water loss near the rims of the globules is efficient, while the inside orbicular structure might have resulted from a longer "interaction" with the globule "solutes" (see text for more detailed information). **d** BSE image emphasizing the relationship between the displayed model and the original sample textures

to suggest the involvement of slab components in the petrogenesis of the FAB recovered in Hole U1440B, water was likely introduced via the assimilation of shallow AOC, as shown by the elevated $^{87}Sr/^{86}Sr_i$ of 0.705802 of the andesites. The fact that the FAB units both above and below Unit 6 are considerably less radiogenic $^{87}Sr/^{86}Sr_i$ values (0.703537 to 0.703745 – Li et al. 2019), and that FAB sample in Hole 1440B have on average even lower $^{87}Sr/^{86}Sr_i$ (i.e. 0.703284), make it unlikely that the globular andesites result from a discrete mantle source that has yet to be tapped by any FAB or boninite sampled during IODP Expedition 352. The introduction of water during the assimilation process likely triggered the separation of a hydrous silicate melt into two immiscible liquid phases, a fluid-saturated silicate melt and a hydrous fluid (Fig. 10a). At this stage, fluid-mobile element fractionation, as well as significant B isotope fractionation must have taken place, with the fluid developing higher $\delta^{11}B$ signatures than the co-existing andesitic melt. The fluid then begins to lose its more aqueous component, gradually decreasing its water/solute ratio while the system is still at supraliquidus conditions (Fig. 10b). Indeed, fluid escape is suggested by the outward-facing plume like structures on the outside of the globules (Fig. 5a). Fluid exsolution and subsequent loss of its more H_2O-rich component will undoubtedly trigger undercooling due to a raising of the solidus of the system, which enables the spherulitic crystallization identified in the Unit 6 globular andesites (Lowenstern et al. 1997; Hort 1998; Annen et al. 2005; Johnson et al. 2008; Roberge et al. 2009). Undercooling must have been sufficiently high to drive spherulitic crystallization to the point where the spherulites were forced to impinge along more or less straight boundaries (see supplement Fig. S9). Ubiquitous and continuous spherulitic crystallization within the andesitic groundmass and the globules requires, that at the point of quenching of both the silicate melt and the solute-bearing fluid, clinopyroxene-saturation was reached, explaining the presence of this mineral in all textural domains (Fig. 10c). Spherulitic crystallization of clinopyroxene is consistent

Hydrous solute-bearing fluid | Silicate melt

with isothermal undercooling between 50 to 90 °C (Lofgren 1974). If water loss is indeed responsible for undercooling, then the loss of ca. 1 wt% H_2O should be sufficient to shift the solidus of either basalt or andesite by a large enough margin to trigger quenching. Indeed, modelling carried out using the rhyolite-MELTS algorithm (Gualda et al. 2012) yields 100 °C of undercooling when ca. 1 wt% H_2O are assumed to have been degassed from an andesite at low

pressure (i.e. less than 100 MPa) and at temperatures ranging between ca. 1050 and 950 °C. The results of this modelling are consistent with fluid loss taking place near the top of the sequence sampled by Hole U1440B where pressure was undoubtedly lower. Furthermore, the absence of plagioglase from the andesitic groundmass, coupled with the ubiquity of clinopyroxene, supports the suppression of plagioclase crystallization due to the presence of water dissolved in silicate melt (cf. Almeev et al. 2012; Sisson and Grove 1993; Danyushevsky 2001). The interface is strongly depleted in sodium by a factor of ten relative to the andesitic groundmass. Hydrothermal glass corrosion experiments show that sodium is easily leached from silicate glasses (cf. Dohmen et al. 2013—Figs. 1 and 3). The depletion of sodium relative to the andesitic groundmass is a strong argument for the involvement of a fluid in the formation of the interface. The direct involvement of seawater can be excluded, as it has been shown that seawater hydrothermal alteration along fractures and fissures results in the incorporation of Cl into secondary mineral phases (van der Zwan et al. 2015, 2012; Barnes and Cisneros 2012; Hart et al. 1974), whereas in the Unit 6 globular andesites, Cl is depleted in the interface and globules relative to the andesitic groundmass (cf. Fig. 6c). Moreover, seawater involvement would have resulted in the addition of Sr into Ca-rich alteration phases (cf. Menzies and Seyfried Jr 1979), which is not the case as all textural domains are Sr-poor (i.e. between 30 to 60 μg/g—see Table 2). As such, the hydrous fluid that led to the formation of the interface must have been hydrothermal in origin to be able to leach Cl from the glass (Seyfried Jr et al. 1986).

Based on the bulk of the geochemical and textural evidence, the globules could represent the solute remnants of a magmatic fluid, and the escape of its more aqueous-rich component leached the andesitic groundmass and stripped it of its Cl and Na content, leading to the formation of the interface (Fig. 10c). This is also supported by the spatial distribution of the interface, which is unmistakably linked to the globules, as has been identified in the 3D X-ray microtomography (Fig. 5). The prominent microscopic orbicular texture in the centre of the globules was likely caused by an auto-metasomatic overprint, resulting from interaction between the escaping fluid and the "globule material" (Fig. 10c, d). In the experimental devitrification study of Lofgren (1971) a comparable orb texture was identified that exclusively formed at conditions above 500 °C and under the presence of alkaline aqueous solutions. Potassium-rich feldspar was found to be a typical de-vitrification product in these experiments. A single alkali feldspar composition with intermediate Na/K ratios has been identified in the globule matrix so that an estimated minimum temperature of ca. 660 °C must have been prevalent during the auto-metasomatic reaction between the remaining fluid and its solute, leading to the formation of the orb texture (Lofgren 1971; Tuttle

and Bowen 1958). Even though the bulk of each globule lost most, if not all of its water, the isolated filled voids found within the globules may represent remnants of the water-rich fluid component (Fig. 10c, d), although this is admittedly highly speculative. In addition to some hydrous mineral phases (e.g. zeolite), cristobalite has been identified in these voids (cf. Fig. 4g, Fig. 5a), a phase that was also identified in the experimental run products of Lofgren (1971).

In conclusion, fluid-melt immiscibility is the process that can explain the majority the geochemical and textural characteristics of the globular andesites from Unit 6 of Hole U1440B. However, this possibility has some very important issues that prevent us from wholeheartedly supporting it. For example, even though there is indirect evidence of the actions of a fluid, as shown by textural evidence and elemental and isotope fractionation, the main component that would have driven these phenomena, water, is almost entirely absent. The absence of water from the globules and andesitic groundmass is puzzling, and one can only speculate that because fluid exsolution took place at high temperature, water loss was extremely efficient. The absence of plagioclase crystallites from the andesitic groundmass is consistent with the presence of water in the system (cf. Almeev et al. 2012; Sisson and Grove 1993; Danyushevsky 2001); however, it is difficult to understand how the andesitic groundmass could have lost the bulk of its water content as it quenched at seafloor pressures (ca. 50 MPa). Perhaps the most problematic aspect of this possibility is the composition of the globules. Previous experimental studies have pointed out that magmatic fluids are dilute and their solutes tend to be dominated by silica and alkali, and to a lesser extent Al and Ca, yet depleted in Mg and Fe (e.g. Shen and Keppler 1997; Manning 2004), which is not fully reflected by the Izu-Bonin samples. Indeed, there appears to be a disconnect between the compelling evidence from various sources (Sr and B isotopes, fluid-mobile trace element systematics, textural evidence, etc.) that support the possibility of fluid-melt immiscibility, and the fact that the major element composition of neither globules nor the andesitic groundmass have the major element compositions expected from a solute derived from a magmatic fluid. Another important problem with the possibility of fluid-melt immiscibility is the fact that fluids are expected to be water-rich (see Shen and Keppler 1997; Allabar and Nowak 2018; Allabar et al. 2020) at the low pressures prevalent in the Izu–Bonin–Mariana oceanic crust (150–50 MPa), which would imply very high water/solute ratios. High water/solute ratios are hard to reconcile with the textural evidence, as the interface, which presumably formed as fluids escaped during the immiscibility process is less volumetric then the globules themselves. It should be pointed out, however, that sample recovery during boring at the levels immediately above unit 6 in Hole 1440B was poor (as low as 9%—Reagan et al. 2015). Based on this

information it is possible that the poor recovery might be associated with the weakening of crustal material resulting from the escape of a large amount of fluid, but this is, of course, mere speculation. These issues highlight the difficulty in interpreting complex textures in magmatic systems *a posteriori*, and further study of similar occurrences is necessary to fully understand how such globular samples form. In particular, additional experimental work that investigates the full range of geochemical and isotope consequences of fluid-melt immiscibility is thus essential to address this disconnect, and to test whether this process can result in appreciable geochemical fractionation as seen in our samples.

Conclusions

Assuming that the globular andesites found in Unit 6 are indeed the result of fluid-melt immiscibility, then the globules are either the remnants of the solute from an immiscible magmatic fluid, in which case they retain the geochemical characteristics of the assimilated altered oceanic crust (i.e. high K_2O, Tl, $^{87}Sr/^{86}Sr_i$, etc.), or they are relicts of AOC that somehow adopted a equidimensional spherical shape that is redolent of immiscibility. Nevertheless, the introduction of water into this magmatic system must have happened at a shallow level through AOC assimilation, and most of the geochemical characteristics of the globules (high K_2O, and B contents) seem to have been inherited from AOC. We stress that these andesitic samples occur in a single small horizon (Unit 6) in Hole U1440B, and there is no evidence to suggest that these are widespread. It could well be that globular textures that form as a result of fluid-immiscibility are more prevalent during the evolution of fluid-bearing lavas, like volcanic arc lavas, but this is by no means certain. These globular samples are highly susceptible to weathering, especially in as much as the porous and devitrified interface is concerned. As such, it is likely that globular andesites or basalt may also occur elsewhere, but are simply not preserved with subsequent weathering. The fact that these samples were recovered in situ via drilling likely contributed to their preservation. Regardless of the nature of the magmatic fluid, the andesitic groundmass exhibits fluid-soluble trace element patterns close to those of MORB, yet the globules show a considerable fluid contribution. These differences in the fluid-mobile trace element budget between the globules and the andesitic groundmass could have resulted from the separation of a hydrous, solute-bearing fluid phase from silicate melt. While other possibilities to explain these textural and geochemical characteristics of our samples cannot be fully excluded (i.e. magma mingling, vesicle segregation), the fluid-melt immiscibility explains the bulk of the characteristics of the globular andesites found in Unit 6 of Hole 1440B, even if this possibility is not without its problems. Additional work is needed, namely, experimental work testing fluid-melt immiscibility under similar circumstances, so that this and other hypotheses can be fully tested.

References

Allabar A, Nowak M (2018) Message in a bottle: spontaneous phase separation of hydrous Vesuvius melt even at low decompression rates. Earth Planet Sci Lett 501:192–201

Allabar A, Gross ES, Nowak M (2020) The effect of initial H_2O concentration on decompression-induced phase separation and degassing of hydrous phonolitic melt. Contrib Mineral Petrol 175(3):22

Almeev RR, Holtz F, Koepke J, Parat F (2012) Experimental calibration of the effect of H2O on plagioclase crystallization in basaltic melt at 200 MPa. Am Mineral 97(7):1234–1240

Anderson AT Jr, Swihart GH, Artioli G, Geiger CA (1984) Segregation vesicles, gas filter-pressing, and igneous differentiation. J Geol 92(1):55–72

Annen C, Blundy J, Sparks R (2005) The genesis of intermediate and silicic magmas in deep crustal hot zones. J Petrol 47(3):505–539

Arevalo R, McDonough WF (2010) Chemical variations and regional diversity observed in MORB. Chem Geol 271(1):70–85

Asiabanha A, Bardintzeff JM (2013) Globule-rich lavas in the Razjerd district, Qazvin, Iran: a unique volcanic fabric. Arab J Geosci 7(5):1907–1925

Ballhaus C, Fonseca ROC, Münker C, Kirchenbaur M, Zirner A (2015) Spheroidal textures in igneous rocks-Textural consequences of H_2O saturation in basaltic melts. Geochim Cosmochim Acta 167:241–252

Barnes JD, Cisneros M (2012) Mineralogical control on the chlorine isotope composition of altered oceanic crust. Chem Geol 326:51–60

Bickle MJ, Teagle DAH (1992) Strontium alteration in the Troodos ophiolite: implications for fluid fluxes and geochemical transport in mid-ocean ridge hydrothermal systems. Earth Planet Sci Lett 113:219–237

Brounce M, Feineman M, LaFemina P, Gurenko A (2012) Insights into crustal assimilation by Icelandic basalts from boron isotopes in melt inclusions from the 1783–1784 Lakagígar eruption. Geochim Cosmochim Acta 94:164–180

Chakraborty S, Dingwell DB, Chaussidon M (1993) Chemical diffusivity of boron in melts of haplogranitic composition. Geochim Cosmochim Acta 57(8):1741–1751

Charlier B, Grove TL (2012) Experiments on liquid immiscibility along tholeiitic liquid lines of descent. Contrib Mineral Petrol 164(1):27–44

Charlier B, Namur O, Grove TL (2013) Compositional and kinetic controls on liquid immiscibility in ferrobasalt-rhyolite volcanic and plutonic series. Geochim Cosmochim Acta 113:79–93

Cichy SB, Botcharnikov RE, Holtz F, Behrens H (2010) Vesiculation and microlite crystallization induced by decompression: a case study of the 1991–1995 Mt Unzen eruption (Japan). J Petrol 52(7–8):1469–1492

Danyushevsky LV (2001) The effect of small amounts of H_2O on crystallisation of mid-ocean ridge and backarc basin magmas. J Volcanol Geotherm Res 110(3–4):265–280

Dohmen L, Lenting C, Fonseca ROC, Nagel T, Heuser A, Geisler T, Denkler R (2013) Pattern formation in silicate glass corrosion zones. Int J Appl Glass Sci 4(4):357–370

Drelich J, Fang C, White C (2002) Measurement of interfacial tension in fluid-fluid systems. Encycl Surf Colloid Sci 3:3158–3163

Ferguson J, Currie K (1972) Silicate Immiscibility in the Ancient "Basalts" of the Barberton Mountain Land, Transvaal. Nature 235:86–89

Fonseca ROC, Kirchenbaur M, Ballhaus C, Münker C, Zirner A, Gerdes A, Heuser A, Botcharnikov R, Lenting C (2017) Fingerprinting fluid sources in Troodos ophiolite complex orbicular glasses using high spatial resolution isotope and trace element geochemistry. Geochim Cosmochim Acta 200:145–166

Gangjian W, Jingxian W, Ying L, Ting K, Zhongyuan R, Jinlong M, Yigang X (2013) Measurement on high-precision boron isotope of silicate materials by a single column purification method and MC-ICP-MS. J Anal Atom Spectrom 28(4):606–612

Gélinas L, Brooks C, Trzcienski W Jr (1976) Archean variolites—quenched immiscible liquids. Can J Earth Sci 13(2):210–230

Gibson I, Beslier M, Cornen G, Milliken K, Seifert K (1996) Major- and trace-element seawater alteration profiles in serpentinite formed during the development of the Iberia Margin, Site 897. In: Proceedings of the Ocean Drilling Program scientific results, pp 519–528

Gualda GA, Ghiorso MS, Lemons RV, Carley TL (2012) Rhyolite-MELTS: a modified calibration of MELTS optimized for silica-rich, fluid-bearing magmatic systems. J Petrol 53(5):875–890

Hanski E (1993) Globular ferropicritic rocks at Pechenga, Kola Peninsula (Russia): liquid immiscibility versus alteration. Lithos 29(3–4):197–216

Harris M, Coggon RM, Smith-Duque CE, Cooper MJ, Milton JA, Teagle DAH (2015) Channelling of hydrothermal fluids during the accretion and evolution of the upper oceanic crust: Sr isotope evidence from ODP Hole 1256D. Earth Planet Sci Lett 416:56–66

Hart S, Erlank A, Kable E (1974) Sea floor basalt alteration: some chemical and Sr isotopic effects. Contrib Mineral Petrol 44(3):219–230

Hervig RL, Moore GM, Williams LB, Peacock SM, Holloway JR, Roggensack K (2002) Isotopic and elemental partitioning of boron between hydrous fluid and silicate melt. Am Mineral 87:769–774

Hort M (1998) Abrupt change in magma liquidus temperature because of volatile loss or magma mixing: effects on nucleation, crystal growth and thermal history of the magma. J Petrol 39(5):1063–1076

Hou T, Veksler IV (2015) Experimental confirmation of high-temperature silicate liquid immiscibility in multicomponent ferrobasaltic systems. Am Mineral 100(5–6):1304–1307

Hughes CJ (1977) Archean variolites—quenched immiscible liquids: discussion. Can J Earth Sci 14(1):137–139

Jarosewich E, Nelen J, Norberg JA (1980) Reference samples for electron microprobe analysis. Geost Geoanal Res 4(1):43–47

Jochum KP, Weis U, Stoll B, Kuzmin D, Yang Q, Raczek I, Jacob DE, Stracke A, Birbaum K, Frick DA et al (2011a) Determination of reference values for NIST SRM 610–617 glasses following ISO guidelines. Geost Geoanal Res 35:397–429

Jochum KP, Wilson SA, Abouchami W, Amini M, Chmeleff J, Eisenhauer A, Hegner E, Iaccheri LM, Kieffer B, Krause J et al (2011b) GSD-1G and MPI-DING reference glasses for in situ and bulk isotopic determination. Geostand Geoanal Res 35:193–226

Johnson ER, Wallace PJ, Cashman KV, Granados HD, Kent AJ (2008) Magmatic volatile contents and degassing-induced crystallization at Volcán Jorullo, Mexico: implications for melt evolution and the plumbing systems of monogenetic volcanoes. Earth Planet Sci Lett 269(3):478–487

Kasemann SA, Meixner A, Rocholl A, Vennemann T, Rosner M, Schmitt AK, Wiedenbeck M (2001) Boron and oxygen isotopic composition of certified reference materials NIST SRM 610/612 and reference materials JB-2 and JR-2. Geostand Newslett 25:405–416

Krassivskaya I, Sharkov E, Bortnikov N, Chistyakov A, Trubkin N, Golovanova T (2009) Variolitic lavas in the axial rift of the mid-atlantic ridge and their origin (Sierra Leone area, 6° 18' N). Petrology 18(3):263–277

Lafuente B, Downs RT, Yang H, Stone N (2016) The power of databases: the RRUFF project. In: Armbruster T, Danisi R (eds) Highlights in mineralogical crystallography. W. de Gruyter GmbH, Berlin, pp 1–30

Lester GW, Clark AH, Kyser TK, Naslund HR (2013) Experiments on liquid immiscibility in silicate melts with H_2O, P, S, F and Cl: implications for natural magmas. Contrib Mineral Petrol 166(1):329–349

Li HY, Taylor RN, Prytulak J, Kirchenbaur M, Shervais JW, Ryan JG, Godard M, Reagan MK, Pearce JA (2019) Radiogenic isotopes document the start of subduction in the Western Pacific. Earth Planet Sci Lett 518:197–210

Lofgren G (1971) Spherulitic textures in glassy and crystalline rocks. J Geophys Res 76(23):5635–5648

Lofgren G (1974) An experimental study of plagioclase crystal morphology; isothermal crystallization. Am J Sci 274(3):243–273

Longerich HP, Jackson SE, Günther D (1996) Inter-laboratory note. Laser ablation inductively coupled plasma mass spectrometric transient signal data acquisition and analyte concentration calculation. J Anal Atom Spectrom 11:899–904

Lowenstern JB, Clynne MA, Bullen TD (1997) Comagmatic A-type granophyre and rhyolite from the Alid volcanic center, Eritrea, northeast Africa. J Petrol 38(12):1707–1721

Lowenstern JB, van Hinsberg V, Berlo K, Liesegang M, Iacovino K, Bindeman IN, Wright HM (2018) Opal-a in glassy pumice, acid alteration, and the 1817 phreatomagmatic eruption at Kawah Ijen (Java), Indonesia. Front Earth Sci 6:11

Manning CE (2004) The chemistry of subduction-zone fluids. Earth Planet Sci Lett 223(1):1–16

Marien CS, Elis JE, Garbe-Schönberg CD, Münker C (2019) Petrogenesis of plagiogranites from the Troodos Ophiolite Complex. Cyprus Contrib Mineral Petrol 174:35

Marschall HR (2018) Boron isotopes in the ocean floor realm and the mantle. In: Horst R (ed) Boron isotopes. Springer, Berlin, pp 189–215

Marschall HR, Wanless VD, Shimizu N, von Strandmann PAP, Elliott T, Monteleone BD (2017) The boron and lithium isotopic composition of mid-ocean ridge basalts and the mantle. Geochim Cosmochim Acta 207:102–138

Marxer H, Bellucci P, Nowak M (2015) Degassing of H_2O in a phonolitic melt: a closer look at decompression experiments. J Volcanol Geothermal Res 297:109–124

McIntosh IM, Llewellin E, Humphreys MCS, Nichols ARL, Burgisser A, Schipper CI, Larsen JF (2014) Distribution of dissolved water in magmatic glass records growth and resorption of bubbles. Earth Planet Sci Lett 401:1–11

Menzies M, Seyfried W Jr (1979) Basalt-seawater interaction: trace element and strontium isotopic variations in experimentally altered glassy basalt. Earth Planet Sci Lett 44(3):463–472

Moore JG (1970) Water content of basalt erupted on the ocean floor. Contrib Mineral Petrol 28(4):272–279

Moore JG, Schilling JG (1973) Vesicles, water, and sulfur in Reykjanes Ridge basalts. Contrib Mineral Petrol 41(2):105–118

Mungall JE, Su S (2005) Interfacial tension between magmatic sulfide and silicate liquids: constraints on kinetics of sulfide liquation and sulfide migration through silicate rocks. Earth Planet Sci Lett 234(1):135–149

Nebel O, Mezger K, Scherer E, Münker C (2005) High precision determinations of $^{87}Rb/^{85}Rb$ in geologic materials by MC-ICP-MS. Int J Mass Spectrom 246(1–3):10–18

Nielsen SG, Rehkämper M, Teagle DA, Butterfield DA, Alt JC, Halliday AN (2006) Hydrothermal fluid fluxes calculated from the isotopic mass balance of thallium in the ocean crust. Earth Planet Sci Lett 251(1):120–133

Pauly BD, Williams LB, Hervig RL, Schiffman P, Zierenberg RA (2014) Methods for in situ SIMS microanalysis of Boron and its isotopes in palagonite. Clay Miner 62(3):224–234

Philpotts AR (1977) Archean variolites - quenched immiscible liquids: discussion. Can J Earth Sci 14(1):139–144

Philpotts AR (1982) Compositions of immiscible liquids in volcanic rocks. Contrib Mineral Petrol 80(3):201–218

Philpotts AR (2008) Comments on: liquid immiscibility and the evolution of basaltic magma. J Petrol 49(12):2171–2175

Polat A, Frei R, Fryer B, Appel PW (2009) The origin of geochemical trends and Eoarchean (ca. 3700 Ma) zircons in Mesoarchean (ca. 3075 Ma) ocelli-hosting pillow basalts, Ivisaartoq greenstone belt, SW Greenland: Evidence for crustal contamination versus crustal recycling. Chem Geol 268(3):248–271

Prytulak J, Brett A, Webb M, Plank T, Rehkämper M, Savage P, Woodhead J (2017) Thallium elemental behavior and stable isotope fractionation during magmatic processes. Chem Geol 448:71–83

Reagan MK, Ishizuka O, Stern RJ, Kelley KA, Ohara Y, Blichert-Toft J, Bloomer SH, Cash J, Fryer P, Hanan BB et al (2010) Fore-arc basalts and subduction initiation in the Izu-Bonin-Mariana system. Geochem Geophy Geosy. https://doi.org/10.1029/2009GC002871

Reagan MK, Pearce JA, Petronotis K, Almeev R, Avery AA, Carvallo C, Chapman T, Christeson GL, Ferré EC, Godard M et al (2015) Expedition 352 summary. Proc Int Ocean Discov Program 352:1–32

Reagan MK, Pearce JA, Petronotis K, Almeev RR, Avery AJ, Carvallo C, Chapman T, Christeson GL, Ferré EC, Godard M et al (2017) Subduction initiation and ophiolite crust: new insights from IODP drilling. Int Geol Rev 59(11):1439–1450

Reagan MK, Heaton DE, Schmitz MD, Pearce JA, Shervais JW, Koppers AA (2019) Forearc ages reveal extensive short-lived and rapid seafloor spreading following subduction initiation. Earth Planet Sci Lett 506:520–529

Roberge J, Delgado-Granados H, Wallace PJ (2009) Mafic magma recharge supplies high CO_2 and SO_2 gas fluxes from Popocatépetl volcano, Mexico. Geology 37(2):107–110

Rosner M, Meixner A (2004) Boron isotopic composition and concentration of ten geological reference materials. Geost Geoanal Res 28(3):431–441

Sandstå NR, Robins B, Furnes H, De Wit M (2011) The origin of large varioles in flow-banded pillow lava from the Hooggenoeg Complex, Barberton Greenstone Belt, South Africa. Contrib Mineral Petrol 162(2):365–377

Sato H (1978) Segregation vesicles and immiscible liquid droplets in ocean-floor basalt of Hole 396B, IPOD/DSDP Leg 46. Initial Reports of the Deep Sea Drilling Project 46:283–291

Sensarma S, Palme H (2013) Silicate liquid immiscibility in the ~ 2.5 Ga Fe-rich andesite at the top of the Dongargarh large igneous province (India). Lithos 170:239–251

Seyfried W Jr, Berndt ME, Janecky D (1986) Chloride depletions and enrichments in seafloor hydrothermal fluids: constraints from experimental basalt alteration studies. Geochim Cosmochim Acta 50(3):469–475

Shen AH, Keppler H (1997) Direct observation of complete miscibility in the albite-H_2O system. Nature 385(6618):710–712

Shervais JW, Reagan MK, Haugen E, Almeev R, Pearce J, Prytulak J, Ryan JG, Whattam S, Godard M, Chapman T, Li H, Kurz W, Nelson WR, Heaton D, Kirchenbaur M, Shimizu K, Sakuyama T, Li Y, Vetter SK (2018) Whole rock geochemistry of Forearc Basalts from IODP Sites 352. PANGAEA https://doi.pangaea.de/10.1594/PANGAEA.895122

Shervais JW, Reagan MK, Haugen E, Almeev R, Pearce J, Prytulak J, Ryan JG, Whattam S, Godard M, Chapman T, Li H, Kurz W, Nelson WR, Heaton D, Kirchenbaur M, Shimizu K, Sakuyama T, Li Y, Vetter SK (2019) Magmatic response to subduction initiation, Part I: fore-arc basalts of the Izu-Bonin Arc from IODP expedition 352. Geochem Geophy Geosy 20:314–338

Shishkina TA, Botcharnikov RE, Holtz F, Almeev RR, Portnyagin MV (2010) Solubility of h_2o-and co_2-bearing fluids in tholeiitic basalts at pressures up to 500 mpa. Chem Geol 277(1–2):115–125

Sisson TW, Grove TL (1993) Experimental investigations of the role of H_2O in calc-alkaline differentiation and subduction zone magmatism. Contrib Mineral Petrol 113(2):143–166

Smith HJ, Spivack AK, Staudigel H, Hart SR (1995) The boron isotopic composition of altered oceanic crust. Chem Geol 126:119–135

Smith RE (1967) Segregation vesicles in basaltic lava. Am J Sci 265(8):696–713

Snyder D, Crambes C, Tait S, Wiebe RA (1997) Magma mingling in dikes and sills. J Geol 105(1):75–86

Stern RJ, Fouch MJ, Klemperer SL (2003) An overview of the Izu-Bonin-Mariana subduction factory. In: John E (ed) Inside the subduction factory. American Geophysical Union, Washington, pp 175–222

Tuttle OF, Bowen NL (1958) Origin of granite in the light of experimental studies in the system $NaAlSi_3O_8$-$KAlSi_3O_8$-SiO_2-H_2O. Geol Soc Am Mem 74:1–146

Veksler IV (2004) Liquid immiscibility and its role at the magmatic-hydrothermal transition: a summary of experimental studies. Chem Geol 210(1):7–31

Veksler IV, Kähn J, Franz G, Dingwell DB (2010) Interfacial tension between immiscible liquids in the system K_2O-FeO-Fe_2O_3-Al_2O_3-SiO_2 and implications for the kinetics of silicate melt unmixing. Am Mineral 95(11–12):1679–1685

Vetere F, Iezzi G, Behrens H, Holtz F, Ventura G, Misiti V, Cavallo A, Mollo S, Dietrich M (2015) Glass forming ability and

crystallisation behaviour of sub-alkaline silicate melts. Earth-Sci Rev 150:25–44

Wanless V, Perfit M, Ridley W, Klein E (2010) Dacite petrogenesis on mid-ocean ridges: evidence for oceanic crustal melting and assimilation. J Petrol 51(12):2377–2410

van der Zwan FM, Fietzke J, Devey CW (2012) Precise measurement of low (< 100 ppm) chlorine concentrations in submarine basaltic glass by electron microprobe. J Anal Atom Spectrom 27(11):1966–1974

van der Zwan FM, Devey CW, Augustin N, Almeev RR, Bantan RA, Basaham A (2015) Hydrothermal activity at the ultraslow-to slow-spreading Red Sea Rift traced by chlorine in basalt. Chem Geol 405:63–81

Affiliations

Raúl O. C. Fonseca[1] · Lina T. Michely[2] · Maria Kirchenbaur[3] · Julie Prytulak[4] · Jeffrey Ryan[5] · Kerstin Hauke[6] · Felipe P. Leitzke[7] · Renat R. Almeev[3] · Chris S. Marien[8] · Axel Gerdes[9] · Rico Schellhorn[6]

[1] Institut für Geologie, Mineralogie und Geophysik, Ruhr-Universität Bochum, 44801 Bochum, Germany

[2] Agroislab GmbH, Prof.-Rehm-Str. 6, 52428 Jülich, Germany

[3] Institut für Mineralogie, Leibniz Universität Hannover, 30167 Hannover, Germany

[4] Science Labs, Department of Earth Sciences, Durham University, Durham DH1 3LE, UK

[5] School of Geosciences, University of South Florida, Tampa, USA

[6] Institut für Geowissenschaften, Universität Bonn, Meckenheimer Allee 169, 53115 Bonn, Germany

[7] Laboratório de Geologia Isotópica, Universidade Federal do Rio Grande do Sul, Av. Bento Gonçalves, Porto Alegre, RS 9500, Brasil

[8] Institut für Geologie und Mineralogie, Universität zu Köln, 50674 Köln, Germany

[9] Institut für Geowissenschaften - Frankfurt Isotope and Element Research Center (FIERCE), Goethe Universität Frankfurt, Altenhöferallee 1, 60438 Frankfurt am Main, Germany